A first-principle predictive theory for a sphere falling through sharply stratified fluid at low Reynolds number

ROBERTO CAMASSA[1], CLAUDIA FALCON[1], JOYCE LIN[2]†, RICHARD M. McLAUGHLIN[1] AND NICHOLAS MYKINS[1]

[1]Department of Mathematics, University of North Carolina at Chapel Hill, Chapel Hill, NC 27599, USA
[2]Department of Mathematics, University of Utah, Salt Lake City, UT 84112, USA

A sphere exhibits a prolonged residence time when settling through a stable stratification of miscible fluids due to the deformation of the fluid-density field. Using a Green's function formulation, a first-principles numerically assisted theoretical model for the sphere–fluid coupled dynamics at low Reynolds number is derived. Predictions of the model, which uses no adjustable parameters, are compared with data from an experimental investigation with spheres of varying sizes and densities settling in stratified corn syrup. The velocity of the sphere as well as the deformation of the density field are tracked using time-lapse images, then compared with the theoretical predictions. A settling rate comparison with spheres in dense homogeneous fluid additionally quantifies the effect of the enhanced residence time. Analysis of our theory identifies parametric trends, which are also partially explored in the experiments, further confirming the predictive capability of the theoretical model. The limit of infinite fluid domain is considered, showing evidence that the Stokes paradox of infinite fluid volume dragged by a moving sphere can be regularized by density stratifications. Comparisons with other possible models under a hierarchy of additional simplifying assumptions are also presented.

Key words: particle/fluid flows, Stokesian dynamics, stratified flows

1. Introduction

In the environment, understanding the behaviour of immersed falling particles is often compounded by steep density gradients in the surrounding medium. Particulate matter has been found to aggregate in regions of sharp stratification caused by haloclines and thermoclines in the ocean and atmosphere (MacIntyre, Alldredge & Gottschalk 1995; Condie & Bormans 1997; Sutor & Dagg 2008). Prolonged settling rates affect many aspects of sedimentation, such as pollution-clearing times (Kellogg 1980; Turco *et al.* 1990), vertical distribution of marine snow (MacIntyre *et al.* 1995; Widder *et al.* 1999), hyperpycnal plume formation in riverine outflows (Parsons, Bush & Syvitski 1995), and can even help to determine the dispersion behaviour and population growth of an organism (Denman & Gargett 1995; Condie & Bormans 1997). The mechanisms behind a settling organism in variable density fluid, which

† Email address for correspondence: joyce.lin@utah.edu

have yet to be fully explored, will provide insight into its evolutionary adaptation. This problem can also be applied to other geophysical phenomena. For example, the movement of plume heads through layers of the Earth's mantle has been shown to be a possible cause of flood basalt events (Bercovici & Mahoney 1994; Jurine *et al.* 2005).

Stratification of immiscible fluids, where surface tension plays a dominant role, has received some attention (see e.g. Manga & Stone 1995; Akers & Belmonte 2006). The available literature providing the underlying dynamics for settling in stratifications of miscible fluids, however, is sparse, though this is the natural medium for environmental applications. Srdić-Mitrović, Mohamed & Fernando (1999) found an increased drag on a sphere settling through sharply stratified fluids at moderate Reynolds number. At a higher Reynolds number, Abaid *et al.* (2004) explored cases in which a falling sphere will levitate and sometimes even reverse direction while passing through regions of high stratification, greatly affecting the settling rate. Recently, Yick *et al.* (2009) provided an experimental study of a sphere settling in a *linear* stratification at low Reynolds number and proposed an enhanced drag coefficient to model the velocity of the system numerically.

In this paper, we bring forth the effect of stratification by studying a single body, a sphere, falling through a miscible, stable density transition at low Reynolds number, which is a relevant regime for a wide range of bio- and geo-physical applications. Similar to the higher-Reynolds-number experiments, we find that a sphere exhibits a prolonged settling rate and slows down substantially through a sharply stratified fluid. Unlike previous studies that have focused only on experimental or numerical results, we will provide a theoretical understanding of the dynamics derived from first principles, analysing and extending the model outlined in Camassa *et al.* (2009). Specifically, we focus here on the model's derivation and its predictions with respect to the various parametric regimes identified by the appropriate non-dimensional groups. New experimental results are presented to test some of the theoretical trends, and their most notable mathematical limits are sketched within relevant subsets of the parametric space. In particular, we study the dynamics of the model as the (horizontal) scale of the fluid domain increases towards the free-space limit and extends beyond the length scale of Oseen's correction to the Stokes approximation. This study shows that in the presence of (sharp) stratifications a mechanism of regularization for the Stokes class of paradoxes could exist independently of that based on the fluid's inertia first considered by Oseen (see e.g. Batchelor 1967). Additionally, we investigate a modification of Tanner's result (Tanner 1963) for bottom effects to account for sharp density jumps, which allows for an estimate of time scales of the sphere slowdown. Finally, we probe the range of applicability of simplified models that derive from extreme cases of the force balance laws on which the full model is based.

This paper is organized as follows: §2 presents the experimental set-up, data and discussion of the prolonged residence time through the interface. In §3, we develop the equations behind the fluid–sphere interaction and present our theory on the final equations of motion. Section 4 describes the numerics and the results from a direct comparison between theoretical and experimental data. In §5, the behaviour of the sphere moving towards the interface is shown to be approximately that of a sphere approaching a plane of zero vertical velocity, giving rise to a time scale for the sphere's slowdown. This time scale is used in §6, where the trends due to parameter variation are explored along with the extension of the model to free space. We study two other possible models in §7 and summarize our findings in §8.
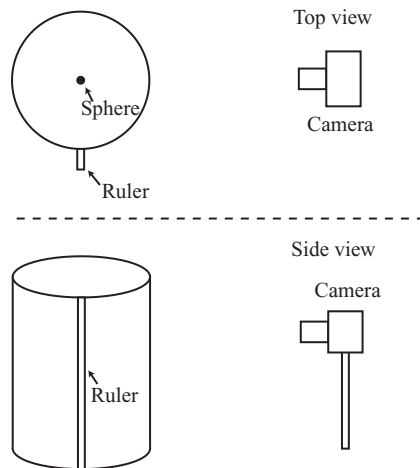
FIGURE 1. Schematic of the experimental set-up.

2. Experiments

2.1. *Methods*

Clear cylindrical Plexiglas tanks with diameters ranging from 6.2 to 18.9 cm and heights of either 31.75 or 52.07 cm are stratified with a top layer of lower-density corn syrup poured over a higher-density (achieved by adding more salt) corn syrup solution. The layers are separately heated, mixed with salt and adjusted with water until homogeneous, and left to degas overnight. Evaporation is minimized by covering free surfaces with airtight membranes and thermal convection is controlled by a thermal bath. By using salt, the density of pure corn syrup can be increased from an approximate density of 1.377 to 1.388 g ml^{-1}. Additionally, this allows us to control the dynamic viscosity variations between the two layers, maintaining them within a less than 0.2 Pa s range, which would not be possible if stratification were to be achieved with water dilution alone. This process yields equal sugar concentration in the top and bottom layers. The constant viscosity range we explore is between 1.6–3.5 Pa s (pure corn syrup is typically 3.5 Pa s at 25 °C). When the top layer is dyed for visualization purposes, an equal volume of water is added to the bottom layer to maintain nearly constant viscosity in the fluid. The dye used is standard water soluble food colouring (either E143 or E129).

Spheres of diameter ranging from 0.08–1.27 cm and densities ranging from 1.360–7.740 g ml^{-1} are released from rest inside the top layer along the centre axis of the tank. Densities and viscosities are measured to within an error of 5×10^{-5} g ml^{-1} and 0.5 %, respectively. For each experiment, photos are taken at specified time intervals with a Nikon D2X or D3 camera aligned along the interfacial plane between the two fluid layers, arranged as in figure 1. Horizontal parallax errors are minimized by centring the tall cylindrical tank with respect to the camera frame, while vertical parallax errors are corrected using the ruler as a fixed scale. By this method, the maximum parallax error is bounded by 1.3 %. Using the image analysis program DataTank, we extract the sphere position from each frame and calculate the velocity using a seven-point least squares scheme.
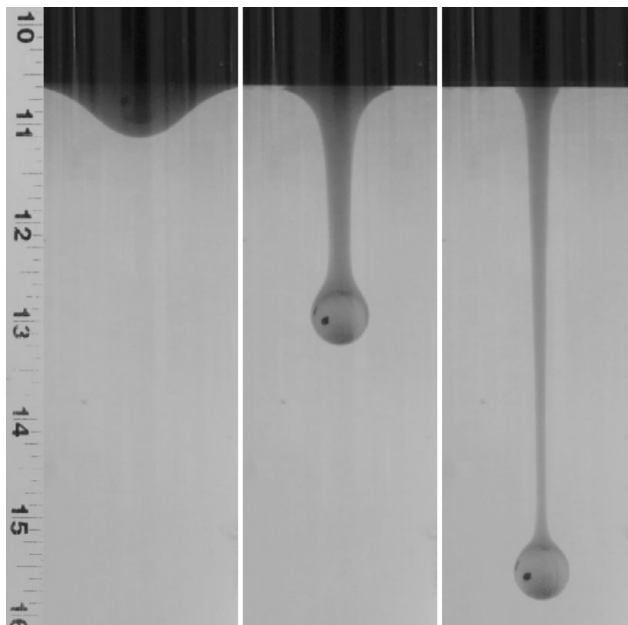
FIGURE 2. Images, corrected for an optical distortion caused by the cylindrical tank, at 40 s intervals of a sphere of radius 0.635 cm falling through a two-layer stratification of densities 1.37661 g cm^{-1} and 1.38384 g ml^{-1} and viscosity $\sim$1.7 Pa s in a cylinder of radius 5.4 cm. Due to the strong change in refractive index across the density transition between the two fluids, the stem boundary appears to have a slight jump in slope.

2.2. *Enhanced residence time*

An immersed translating sphere will entrain ambient fluid, regardless of the viscosity or density variation (for potential inviscid flow this is known as Darwin drift, Darwin 1953, recently analysed in Camassa *et al.* 2008). In the case of a stratified fluid, the entrained fluid is buoyant with respect to the surrounding medium. Figure 2 shows a sphere that has dragged less dense, dyed fluid into the bottom layer. Notice the stem of entrained fluid that persists at long lengths. Unlike the case of immiscible fluids, where surface tension eventually leads to a pinch-off of the stem, for this case of miscible fluids the stem persists in all our experiments and slowly diffuses away long after the sphere settles to the bottom of the container.

Given sufficient depth in each layer, the sphere velocity will change from the terminal velocity in the upper layer to the terminal velocity in the lower layer as it passes through the density transition. However, instead of a monotonic transition which would be imposed if the buoyancy force were to be simply determined by the hydrostatic equilibrium fluid density undistorted by the sphere's motion, the buoyant entrained fluid creates an extra anomalous density force that causes the sphere to slow down beyond the terminal velocity of the lower layer, as seen in figure 3. (The initial acceleration from rest cannot be seen in the velocity plot as it is averaged into the calculation of the derivative of the sphere position.) These data show that the sphere reaches the theoretical terminal velocities computed using the drag force on a sphere for a homogeneous fluid in a pipe (Happel & Byrne 1954) in both the upper and lower layers. It is the slowdown that occurs between these two terminal velocities that we are most interested in capturing.
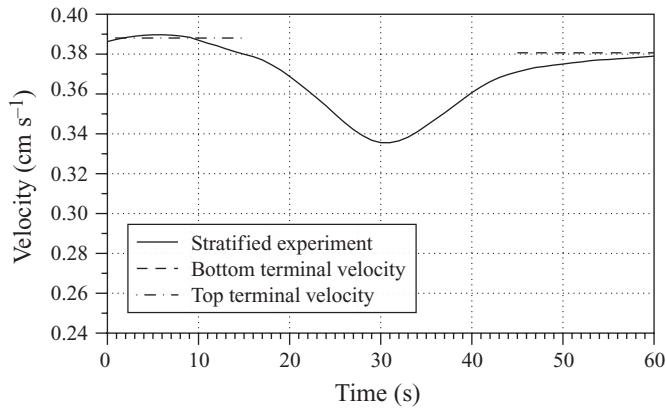
FIGURE 3. Velocity profile of a 0.635 cm radius, 1.46755 g ml^{-1} density sphere falling through a fluid of upper layer density 1.37741 g ml^{-1} and lower layer density 1.37891 g ml^{-1} with viscosity $\sim$1.8 Pa s in a cylindrical tank of radius 9.45 cm. The theoretical terminal velocities are also marked for each layer using the drag force for a sphere falling through homogeneous fluid in a pipe (Happel & Byrne 1954).
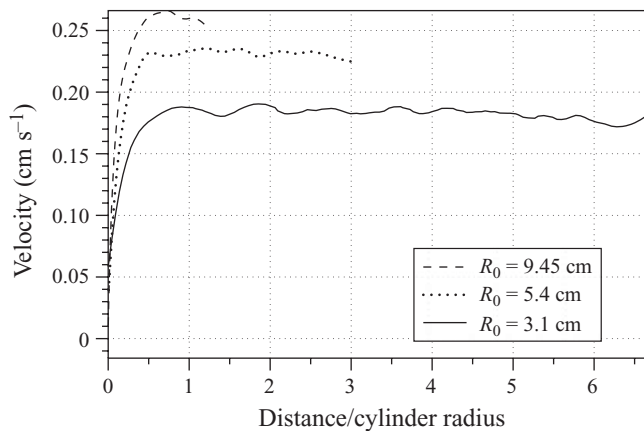

FIGURE 4. Graph of the velocity versus distance to the bottom of a tank for a sphere of radius 0.635 cm and density 1.46755 g ml^{-1} falling in homogeneous fluid of density 1.37955 g ml^{-1} and viscosity $\sim$3.5 Pa s. Distances are normalized with the cylinder radius, R_0.

The local minimum velocity occurs shortly after the sphere enters the lower layer, and this minimum is an indication of a prolonged residence time near the interface between the two layers. All the parameters of the experiment (relative densities, viscosities, sphere and cylinder radii, initial velocity and distance of the sphere to the interface, etc.) play a role in determining the interplay between the buoyant force of the entrained fluid and that of the downward moving sphere.

Tanner (1963) demonstrated that for a sphere falling in a tube with a closed end, the effect of the rigid bottom is negligible when the sphere is outside a cylinder radius from the bottom (see Brenner 1961 for the half-space limit with an infinite bottom). We have explored this trend by tracking a sphere falling through homogeneous fluid in cylinders of varying sizes. The data from this study are consistent with Tanner's results, and are shown in figure 4, where the velocity is plotted as a function of distance to the bottom of the tank, normalized by the cylinder radius, thus demonstrating the role of increasing cylindrical tank radii in making the bottom effect extend further
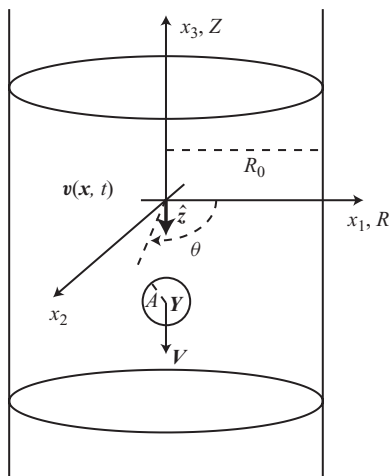
FIGURE 5. Schematic of the theoretical set-up and notation.

into the tank. Hence, in order for the sphere to reach terminal velocity in the top layer, the sphere must be positioned at least one cylinder radius away from the interface, and be able to fall in a region at least one cylinder radius away from the free surface of the fluid. Similarly, the sphere must be allowed to fall in a region at least one cylinder radius away from the interface and the bottom of the tank for the sphere to attain terminal velocity in the bottom layer.

3. Theory

3.1. *Equations of motion*

We begin with the Navier–Stokes equations for an incompressible, Newtonian fluid of velocity $v(x, t)$ and variable density $\rho(x, t)$ at time t and at a point x inside a cylinder of radius R_0 and outside a sphere of radius A (see figure 5) moving with velocity $V(t) = (0, 0, V(t))$

$$\frac{\partial \rho}{\partial t} + v \cdot \nabla \rho = 0, \quad \nabla \cdot v = 0, \tag{3.1}$$

$$\rho \left(\frac{\partial v}{\partial t} + v \cdot \nabla v \right) = \rho \hat{g} - \nabla p + \mu \nabla^2 v, \tag{3.2}$$

$$v = V(t) \quad \text{for } |x - Y(t)| = A, \tag{3.3}$$

$$v = 0 \quad \text{for } \sqrt{x_1^2 + x_2^2} = R_0, \quad -\infty < x_3 < \infty, \tag{3.4}$$

$$v \to 0 \quad \text{for } |x_3| \to \infty, \tag{3.5}$$

where $Y(t)$ is the position of the centre of the sphere in the laboratory frame of reference, so that $\dot{Y}_3(t) = V(t)$. Here $\hat{g}$ is the gravity acceleration vector (with magnitude 981 cm s^{-2}), oriented along the unit vector $\hat{z} \equiv (0, 0, -1)$.

As the fluid density is variable, we define a constant (average) reference density $\rho_{ref} = (\rho_1 + \rho_2)/2$, where ρ_1 is the density of the upper layer and ρ_2 is the density of the lower layer. Thus, we have a non-dimensional density $\tilde{\rho} = \rho/\rho_{ref}$ and a constant kinematic viscosity $v = \mu/\rho_{ref}$. The dimensionless Reynolds, Strouhal and Froude numbers are defined as $Re = AU/v$, $St = A/UT$ and $Fr = U/\sqrt{gA}$, respectively, where U is the terminal velocity of the sphere in a homogeneous fluid of density ρ_{ref}, T is the deceleration time and g is gravity. The non-dimensionalized momentum component

of the incompressible Navier–Stokes equation for the motion of the fluid is

$$Re\,St\,\tilde{\rho}\frac{\partial\tilde{\boldsymbol{v}}}{\partial\tilde{t}} + Re\,\tilde{\rho}\tilde{\boldsymbol{v}}\cdot\tilde{\boldsymbol{\nabla}}\tilde{\boldsymbol{v}} = \frac{Re}{Fr^2}\tilde{\rho}\hat{z} - \tilde{\boldsymbol{\nabla}}\tilde{p} + \tilde{\nabla}^2\tilde{\boldsymbol{v}}, \tag{3.6}$$

with the pressure scaled by $\mu U/A$, and spatial coordinates and time scaled by A and T, respectively. From the experimental parameters, we find that $St \sim O(10^{-1})$, $O(10^{-5}) < Re < O(10^{-2})$ and $O(10^{-1}) < Re/Fr^2 < O(10^3)$. With these bounds, we can scale out the inertial terms, simplifying (3.6) to the Stokes equation with variable density:

$$\tilde{\nabla}^2\tilde{\boldsymbol{v}} = \tilde{\boldsymbol{\nabla}}\tilde{p} - \frac{Re}{Fr^2}\tilde{\rho}\hat{z}. \tag{3.7}$$

Also note that these parameters allow us to show theoretically that the sphere's motion does not generate internal waves (see Appendix A), which is consistent with our laboratory observations. Equation (3.7) can be re-cast in dimensional form and augmented with continuity and incompressibility conditions to give us the full equations of motion for the fluid under the Stokes' approximation,

$$\mu\nabla^2\boldsymbol{v} = \boldsymbol{\nabla}p - \rho\hat{\boldsymbol{g}}, \tag{3.8}$$

$$\boldsymbol{\nabla}\cdot\boldsymbol{v} = 0, \tag{3.9}$$

$$\boldsymbol{v} = \boldsymbol{V}(t) \quad \text{for } |\boldsymbol{x} - \boldsymbol{Y}(t)| = A, \tag{3.10}$$

$$\boldsymbol{v} = 0 \quad \text{for } \sqrt{x_1^2 + x_2^2} = R_0, \ -\infty < x_3 < \infty, \tag{3.11}$$

$$\boldsymbol{v} \to 0 \quad \text{for } |x_3| \to \infty, \tag{3.12}$$

$$\frac{\partial\rho}{\partial t} + \boldsymbol{v}\cdot\boldsymbol{\nabla}\rho = 0. \tag{3.13}$$

In (3.13), we have ignored diffusion of salt, the stratifying agent for our fluid. Over the course of our experiments, we see the persistence of sharp interfaces, made visible by dye, between the upper and lower fluids as well as along the thin stems of upper layer fluid dragged by the sphere. These observations, an example of which can be seen in figure 2, seem to indicate that dye does not diffuse appreciably over the duration of our experiments. Assuming that the diffusivity of dye is comparable to that of salt in our fluid, lack of appreciable diffusion should apply to the stratifying agent as well. We note that for water–salt solutions, the diffusivity of salt (as well as most ionic solutes) is $1.5 \times 10^{-5}\,\mathrm{cm}^2\,\mathrm{s}^{-1}$ (see e.g. Rard & Miller 1979), and there seems to be no reason that this diffusivity would be enhanced in our viscous corn syrup solution. We remark that fluid motion itself, in the form of shear flows, can enhance diffusivity through the mechanism of Taylor dispersion (Taylor 1953), which essentially relies on the stretching of interfaces separating regions from high to low concentrations of diffusing solute. In our experiments, these regions would likely occur in the stem or near the sphere where the shear rate would be highest. However, at least for the range of experimental parameters we have explored, there seems to be little evidence of enhanced diffusion effects, as ultimately borne out by the good agreement between our non-diffusive theory with the experimental data. We tested and corroborated these assumptions further in experimental measurements of a naturally coloured salt, potassium iodide, in corn syrup over a wide range of dilutions with water, as well as theoretically with simple two-dimensional shear calculations. Details are reported in Lin (2009).

The equation of motion for the sphere can be written as

$$m_s\frac{\mathrm{d}\boldsymbol{V}(t)}{\mathrm{d}t} = m_s\hat{\boldsymbol{g}} + \oint_S \boldsymbol{\sigma}\cdot\hat{\boldsymbol{n}}\,\mathrm{d}S, \tag{3.14}$$

where m_s is the mass of the sphere, $\boldsymbol{\sigma}$ is the stress tensor, S is the surface of the sphere and $\hat{\boldsymbol{n}}$ is the outward normal unit vector to this surface.

Taking advantage of the linearity of the Stokes equations, we split the fluid flow into two parts,

$$v(\boldsymbol{x}, t) = \boldsymbol{u}(\boldsymbol{x}, t) + \boldsymbol{w}(\boldsymbol{x}, t). \tag{3.15}$$

The first part, $\boldsymbol{u}(\boldsymbol{x}, t)$, is a Stokes flow in a cylinder with static initial density distribution $\rho_0(x_3) = \rho(\boldsymbol{x}, 0)$, which can be absorbed into the pressure component of the Stokes equations. This velocity will incorporate the boundary conditions on the moving sphere. The second part, $\boldsymbol{w}(\boldsymbol{x}, t)$, which we call the perturbation velocity, satisfies homogeneous boundary conditions and is forced by the (typically small) term $\rho(\boldsymbol{x}, t) - \rho_0(x_3)$. The equation of motion for the sphere becomes

$$m_s \frac{\mathrm{d}\boldsymbol{V}(t)}{\mathrm{d}t} = m_s \hat{\boldsymbol{g}} + \oint_S \boldsymbol{\sigma}_u \cdot \hat{\boldsymbol{n}} \, \mathrm{d}S + \oint_S \boldsymbol{\sigma}_w \cdot \hat{\boldsymbol{n}} \, \mathrm{d}S, \tag{3.16}$$

where $\boldsymbol{\sigma}_u$ and $\boldsymbol{\sigma}_w$ are the stress tensors for $\boldsymbol{u}$ and $\boldsymbol{w}$, respectively. The latter stress tensor $\boldsymbol{\sigma}_w$ originates solely from the advection of the density field, and gives rise to an effective buoyancy-like force, which we refer to as the anomalous density force to distinguish it from the usual Archimedean buoyancy.

3.2. *Stokes flow in a cylinder*

The equations of motion for the velocity component $\boldsymbol{u}(\boldsymbol{x}, t)$ in (3.15), written in the frame of reference moving with the sphere (abusing notation a little, we will not differentiate our notation to distinguish between lab and moving body frame, as long as this does not generate confusion) are

$$\mu \nabla^2 \boldsymbol{u} = \nabla p_s - \rho_0(x_3 + Y_3(t))\hat{\boldsymbol{g}}, \tag{3.17}$$

$$\nabla \cdot \boldsymbol{u} = 0, \tag{3.18}$$

$$\boldsymbol{u} = 0 \quad \text{for } |\boldsymbol{x}| = A, \tag{3.19}$$

$$\boldsymbol{u} = -\boldsymbol{V}(t) \quad \text{for } \sqrt{x_1^2 + x_2^2} = R_0, \quad -\infty < x_3 < \infty, \tag{3.20}$$

$$\boldsymbol{u} \to -\boldsymbol{V}(t) \quad \text{for } |x_3| \to \infty. \tag{3.21}$$

Happel & Byrne (1954) use a method of reflections to decompose the flow into a series

$$\boldsymbol{u} = (\boldsymbol{u}^{(0)} + \boldsymbol{u}^{(1)}) + (\boldsymbol{u}^{(2)} + \boldsymbol{u}^{(3)}) + \cdots, \tag{3.22}$$

where

$$\boldsymbol{u}^{(0)} = -\boldsymbol{V}(t), \tag{3.23}$$

$$\boldsymbol{u}^{(1)} = \begin{cases} -\boldsymbol{u}^{(0)}, & r = A, \\ 0, & r \to \pm\infty, \end{cases} \tag{3.24}$$

$$\boldsymbol{u}^{(2)} = \begin{cases} -\boldsymbol{u}^{(1)}, & R = R_0, \\ 0, & Z \to \pm\infty, \end{cases} \tag{3.25}$$

$$\boldsymbol{u}^{(3)} = \begin{cases} -\boldsymbol{u}^{(2)}, & r = A, \\ 0, & r \to \pm\infty, \end{cases} \tag{3.26}$$

$$\vdots$$

This infinite sum truncated at the *odd-labelled* terms would satisfy the boundary conditions on the sphere, while when the sum is truncated at the *even-labelled* terms the boundary conditions on the cylinder are satisfied. The first term $\boldsymbol{u}^{(0)}$ is a constant flow (in space), whose inclusion changes the frame of reference from the lab frame to a frame of reference moving with the sphere. The second term $\boldsymbol{u}^{(1)}$ satisfies the boundary conditions using a sphere in Stokes flow in free space. Happel & Byrne (1954) provide the full solution for the third term $\boldsymbol{u}^{(2)}$, which cancels out the contribution of $\boldsymbol{u}^{(1)}$ on the boundary of the cylinder. The magnitudes of $\boldsymbol{u}^{(0)}$ and $\boldsymbol{u}^{(1)}$ are $O(1)$ and the sum of the two velocities satisfies the boundary conditions on the sphere. The error incurred on the cylinder walls has magnitude $O(A/R_0)$. The next reflection $\boldsymbol{u}^{(2)}$ has magnitude of order $O(A/R_0)$, and the sum $\boldsymbol{u}^{(0)} + \boldsymbol{u}^{(1)} + \boldsymbol{u}^{(2)}$ satisfies the boundary conditions on the cylinder so that this sum incurs an error on the sphere of order $O(A/R_0)$.

Happel & Byrne do not study the convergence nature of the series from this method of reflections, but notice that each reflection contributes a multiplicative (small) factor A/R_0. To correct for the error made on the sphere by $\boldsymbol{u}^{(2)}$, the next reflection $\boldsymbol{u}^{(3)}$ must be of order $O(A/R_0)$. Thus, $\boldsymbol{u}^{(2)}$ and $\boldsymbol{u}^{(3)}$ have the same order of magnitude. The rest of the terms are not computed explicitly, but we can expect that this pattern be repeated, so that the series expansion $\boldsymbol{u} = (\boldsymbol{u}^{(0)} + \boldsymbol{u}^{(1)}) + (\boldsymbol{u}^{(2)} + \boldsymbol{u}^{(3)}) + \cdots$ decreases by an order of magnitude in pairs, as indicated explicitly by the parenthetical grouping.

To approximate $\boldsymbol{u}$ consistently, we cannot simply use the first three terms $\boldsymbol{u}^{(0)} + \boldsymbol{u}^{(1)} + \boldsymbol{u}^{(2)}$, which are provided explicitly by Happel & Byrne (1954). The interface would pass through the sphere when $\boldsymbol{u}^{(3)}$ is neglected, as this term is of the same order as $\boldsymbol{u}^{(2)}$. While an explicit form of $\boldsymbol{u}^{(3)}$ is not readily available, its most important contribution in the dynamics of the sphere can be obtained by cancelling out the maximum error $-2.10444AV(t)/R_0$ incurred on the sphere with a Stokes flow solution in free space. (Along with the convergence and consistency issues mentioned above, we remark that the asymptotic properties of the reflection series as $A/R_0 \to 0$ are not discussed by Happel & Byrne 1954. The asymptotic ordering of terms in (3.22) would fail near the cylinder boundary, which would require techniques from matched asymptotics to address this non-uniformity in a region near the cylinder's boundary.) With this correction, the second component of the series (3.22) can be re-written as

$$u_Z^{(1)} = -V(t)\left(1 + 2.10444\frac{A}{R_0}\right)\left[\frac{-3A}{4r} - \frac{3AZ^2}{4r^3} - \frac{A^3}{4r^3} + \frac{3Z^2A^3}{4r^5}\right], \qquad (3.27)$$

$$u_R^{(1)} = -V(t)\left(1 + 2.10444\frac{A}{R_0}\right)\left[\frac{-3ARZ}{4r^3} + \frac{3A^3RZ}{4r^5}\right]. \qquad (3.28)$$

Note that by including this cancellation we no longer satisfy the boundary conditions on the sphere or the cylinder exactly, but the violation is consistent with the overall asymptotic error of the retained terms as $A/R_0 \to 0$.

All computations shown in this paper use the above Happel & Byrne's formulation with the additional correction from (3.27) and (3.28). We remark that alternative strategies for approximating homogeneous density Stokes fluid flow induced by a sphere in uniform motion along the axis of a bounding cylinder exist, but we do not explore them in this work, as our focus is on obtaining the correction velocity $\boldsymbol{w}(\boldsymbol{x}, t)$ coming from stratification, for which the homogeneous flow velocity $\boldsymbol{u}(\boldsymbol{x}, t)$ is simply a forcing term through its partial role in the density advection. More accurate approximate solutions for this velocity can likely be obtained, e.g. by using the infinite series formulation in Linton (1995).

The approximate solution for the homogeneous fluid Stokes flow in a cylinder can now be used with variable density and time dependent sphere's velocity to find the drag force due to this flow,

$$\oint_S \boldsymbol{\sigma}_s \cdot \hat{\boldsymbol{n}} \, dS = -\hat{\boldsymbol{g}} \int_{\Omega_s} \rho_0(x_3 + Y_3(t)) \, d\Omega_s - 6\pi A \mu V(t) K, \qquad (3.29)$$

where Ω_s is the sphere domain and $K = (1 - 2.10444(A/R_0) + 2.08877(A/R_0)^3 + \cdots)^{-1}$ is the drag coefficient.

3.3. *Perturbation velocity*

For the stratification-induced flow, we define $\epsilon G(\boldsymbol{x}, t) = (\rho(\boldsymbol{x}, t) - \rho_0(x_3 + Y_3(t)))/\rho_{ref}$ and write the governing equations in a moving frame of reference,

$$\mu \nabla^2 \boldsymbol{w} = \nabla p_w - \epsilon G(\boldsymbol{x}, t) \rho_{ref} \hat{\boldsymbol{g}}, \qquad (3.30)$$

$$\nabla \cdot \boldsymbol{w} = 0, \qquad (3.31)$$

$$\boldsymbol{w} = 0 \quad \text{for } |\boldsymbol{x}| = A, \qquad (3.32)$$

$$\boldsymbol{w} = 0 \quad \text{for } \sqrt{x_1^2 + x_2^2} = R_0, \ -\infty < x_3 < \infty, \qquad (3.33)$$

$$\boldsymbol{w} \to 0 \quad \text{for } |x_3| \to \infty. \qquad (3.34)$$

The boundary conditions for $\boldsymbol{w}$ are homogeneous, and we can find an approximate solution for $\boldsymbol{w}(\boldsymbol{x}, t)$ using the free-space Green's function due to Oseen (1927). This is the solution of the equations

$$\mu \nabla^2 \boldsymbol{W}(\boldsymbol{x}, \boldsymbol{y}) = \nabla P(\boldsymbol{x}, \boldsymbol{y}) - \rho_{ref} \hat{\boldsymbol{g}} \delta(\boldsymbol{x} - \boldsymbol{y}), \qquad (3.35)$$

$$\nabla \cdot \boldsymbol{W} = 0, \qquad (3.36)$$

$$\boldsymbol{W} = 0 \quad \text{for } |\boldsymbol{x}| = A, \qquad (3.37)$$

$$\boldsymbol{W} \to 0 \quad \text{as } |\boldsymbol{x}| \to \infty, \qquad (3.38)$$

for a Stokeslet of strength $\rho_{ref} \hat{\boldsymbol{g}}$ located at the point $\boldsymbol{y}$ outside a rigid sphere of radius A surrounded by an infinite Stokes fluid. The resultant force on the sphere can be computed using the reciprocal theorem (see Appendix D).

We look for an asymptotic expansion $\boldsymbol{w} = \boldsymbol{w}^{(0)} + \boldsymbol{w}^{(1)} + \boldsymbol{w}^{(2)} + \boldsymbol{w}^{(3)} + \cdots$ for small $(\rho(\boldsymbol{x}, t) - \rho_0)/\rho_{ref}$. The first term of order $O(\epsilon A/R_0)$ can be written as the convolution

$$\boldsymbol{w}^{(0)}(\boldsymbol{x}, t) = \int_{\Omega_f} \epsilon G(\boldsymbol{y}, t) \boldsymbol{W}(\boldsymbol{x}, \boldsymbol{y}) \, d\Omega_f, \qquad (3.39)$$

$$p_w^{(0)}(\boldsymbol{x}, t) = \int_{\Omega_f} \epsilon G(\boldsymbol{y}, t) P(\boldsymbol{x}, \boldsymbol{y}) \, d\Omega_f, \qquad (3.40)$$

where Ω_f is the fluid domain.

By interchanging the order of integration (which is allowed because of the convergence properties determined by the integrands), the force calculation for the

first-order approximation becomes

$$
\oint_S \sigma_{w}^{(0)}{}_{ij} n_j \, \mathrm{d}S = \oint_S \left(-p_w^{(0)}\delta_{ij} + \mu \left(\frac{\partial w_i^{(0)}}{\partial x_j} + \frac{\partial w_j^{(0)}}{\partial x_i} \right) \right) n_j \, \mathrm{d}S
$$

$$
= \int_{\Omega_f} \epsilon G(\boldsymbol{y}, t) \oint_S \left(-P(\boldsymbol{x}, \boldsymbol{y})\delta_{ij} + \mu \left(\frac{\partial W_i(\boldsymbol{x}, \boldsymbol{y})}{\partial x_j} + \frac{\partial W_j(\boldsymbol{x}, \boldsymbol{y})}{\partial x_i} \right) \right) n_j \, \mathrm{d}S \, \mathrm{d}\Omega_f
$$

$$
= \int_{\Omega_f} \epsilon G(\boldsymbol{y}, t) \frac{A\rho_{ref}\hat{g}_i}{4} \left\{ \frac{3\left(r^2 + y_3^2\right)}{r^3} + \frac{A^2\left(r^2 - 3y_3^2\right)}{r^5} \right\} \mathrm{d}\Omega_f, \tag{3.41}
$$

where $r = |\boldsymbol{y}|$.

Equations (3.39) and (3.41) determine the first-order approximation to the fluid flow and the resultant force on the sphere due to the density variation.

3.4. *Theoretical model*

Combining the results from §§ 3.2 and 3.3, we have the equation for the vertical component of the velocity of the sphere and the advection of the fluid,

$$
m_s \frac{\mathrm{d}V(t)}{\mathrm{d}t} = m_s g - g \int_{\Omega_s} \rho_0(x_3 + Y_3(t)) \, \mathrm{d}\Omega_s
$$

$$
- 6\pi A\mu V(t)\left(1 - 2.10444(A/R_0) + 2.08877(A/R_0)^3 + \cdots\right)^{-1}
$$

$$
+ \int_{\Omega_f} \epsilon G(\boldsymbol{y}, t) \frac{A\rho_{ref}g}{4} \left\{ \frac{3\left(r^2 + y_3^2\right)}{r^3} + \frac{A^2\left(r^2 - 3y_3^2\right)}{r^5} \right\} \mathrm{d}\Omega_f, \tag{3.42}
$$

$$
\frac{\partial \rho}{\partial t}(\boldsymbol{x}, t) + (\boldsymbol{u}(\boldsymbol{x}, t) + \boldsymbol{w}(\boldsymbol{x}, t)) \cdot \nabla\rho(\boldsymbol{x}, t) = 0. \tag{3.43}
$$

This can be further reduced when written in non-dimensional form,

$$
Re \, St \, \frac{4\pi}{3} \frac{\rho_s}{\rho_{ref}} \frac{\mathrm{d}\tilde{V}(\tilde{t})}{\mathrm{d}\tilde{t}} = \frac{Re}{Fr^2} \left(\frac{4\pi}{3} \frac{\rho_s}{\rho_{ref}} - \int_{\tilde{\Omega}_s} \tilde{\rho}_0(\tilde{x}_3 + \tilde{Y}_3(t)) \, \mathrm{d}\tilde{\Omega}_s \right)
$$

$$
- 6\pi\tilde{V}(\tilde{t})\left(1 - 2.10444(A/R_0) + 2.08877(A/R_0)^3 + \cdots\right)^{-1}
$$

$$
+ \frac{Re}{Fr^2} \int_{\tilde{\Omega}_f} \frac{\epsilon G(\tilde{\boldsymbol{y}}, \tilde{t})}{4} \left\{ \frac{3\left(\tilde{r}^2 + \tilde{y}_3^2\right)}{\tilde{r}^3} + \frac{\left(\tilde{r}^2 - 3\tilde{y}_3^2\right)}{\tilde{r}^5} \right\} \mathrm{d}\tilde{\Omega}_f, \tag{3.44}
$$

which shows that the sphere's acceleration term $\mathrm{d}V/\mathrm{d}t$ can be scaled out. We are left with

$$
\tilde{V}(\tilde{t}) = \frac{Re}{Fr^2} \left(\frac{4\pi}{3} \frac{\rho_s}{\rho_{ref}} - \int_{\tilde{\Omega}_s} \tilde{\rho}_0(\tilde{x}_3 + \tilde{Y}_3(t)) \, \mathrm{d}\tilde{\Omega}_s \right.
$$

$$
\left. + \int_{\tilde{\Omega}_f} \frac{\epsilon G(\tilde{\boldsymbol{y}}, \tilde{t})}{4} \left\{ \frac{3\left(\tilde{r}^2 + \tilde{y}_3^2\right)}{\tilde{r}^3} + \frac{\left(\tilde{r}^2 - 3\tilde{y}_3^2\right)}{\tilde{r}^5} \right\} \mathrm{d}\tilde{\Omega}_f \right) \bigg/ (6\pi K), \tag{3.45}
$$

$$
St \frac{\partial \tilde{\rho}}{\partial \tilde{t}}(\tilde{\boldsymbol{x}}, \tilde{t}) + (\tilde{\boldsymbol{u}}(\tilde{\boldsymbol{x}}, \tilde{t}) + \tilde{\boldsymbol{w}}(\tilde{\boldsymbol{x}}, \tilde{t})) \cdot \tilde{\nabla}\tilde{\rho}(\tilde{\boldsymbol{x}}, \tilde{t}) = 0, \tag{3.46}
$$

where

$$
K = \left(1 - 2.10444(A/R_0) + 2.08877(A/R_0)^3 + \cdots\right)^{-1}. \tag{3.47}
$$

In dimensional form and in the frame of reference moving with the sphere, we have our final equations of motion for the sphere and fluid velocities

$$
\left.
\begin{aligned}
\frac{\mathrm{d}Y_3}{\mathrm{d}t}(t;\rho) = V(t;\rho) &= (6\pi A\mu K)^{-1}\left(m_s g - g \int_{\Omega_s} \rho_0(x_3 + Y_3(t;\rho))\,\mathrm{d}\Omega_s \right. \\
&\left. + \int_{\Omega_f} \epsilon G(\boldsymbol{y},t) \frac{A\rho_{ref}\,g}{4}\left\{ \frac{3\,(r^2 + y_3^2)}{r^3} + \frac{A^2\,(r^2 - 3y_3^2)}{r^5} \right\}\mathrm{d}\Omega_f \right), \\
\frac{\partial\rho}{\partial t}(\boldsymbol{x},t) &+ (\boldsymbol{u}(\boldsymbol{x},t;V) + \boldsymbol{w}(\boldsymbol{x},t;\rho)) \cdot \nabla\rho(\boldsymbol{x},t) = 0.
\end{aligned}
\right\} \quad (3.48)
$$

We remark that the velocities advecting the density in this system satisfy the boundary conditions stated in (3.19)–(3.21) and in (3.32)–(3.34). The detailed formulations for the velocities $\boldsymbol{u} + \boldsymbol{w}$ can be found in Appendices B and C. Equations (3.48) in combination with formulae (B 1)–(B 4) and (C 1) for the approximation to the velocity field constitute our final model for the settling of the sphere with the specified density stratification.

Mathematically, this model is a coupled pair of integro-differential equations in both $\rho(\boldsymbol{x},t)$ and $Y_3(t;\rho)$, where the speed of the sphere $V(t)$ determines $\boldsymbol{u}$ and the density field $\rho(\boldsymbol{x},t)$ determines the domain of integration for $\boldsymbol{w}$. The initial data consist of the initial position of the sphere $Y_3(0)$, and an initial fluid density distribution $\rho_0(x_3)$, inside a cylinder of radius R_0 and outside a sphere of radius A centred along the cylinder axis (where the sphere centre is constrained at all times for axially symmetric solutions). These initial data completely determine the future evolution of the density field by advection through the fluid velocities, whose combination satisfies the rigid boundary conditions (to within the accuracy of the analytic approximations based on Stokes flow theory). In writing the model (3.48), we have added ρ and V to the functional arguments to emphasize the coupling between equations. In the remainder of this work, however, we revert to the previously used standard notation to avoid lengthy argument lists.

4. Results

4.1. *Computation*

Note that because the flow is axisymmetric, we only need to consider half of the vertical cross-section of the cylinder to model the entire system. The Stokes portion $\boldsymbol{u}$ can be separated into temporal and spatial components $V(t)\boldsymbol{f}(\boldsymbol{x})$. The function $\boldsymbol{f}(\boldsymbol{x})$ is computed *a priori* on a two-dimensional grid in the fluid domain of interest.

For a two-layer fluid stratification, we use a step function for the density transition and track points on the interface between the two layers of fluid. For a more diffused stratification, we can track multiple isopycnal lines and interpolate to find the entire density field. Since the system is axisymmetric, these density surfaces are initialized as horizontal lines and advected using an ordinary differential equation solver with the formulation as in (3.48). The velocity $\boldsymbol{u}$ for each tracked point is found by cubic interpolation on the two-dimensional grid computed by $\boldsymbol{f}(\boldsymbol{x})$ and multiplied by the current value of $V(t)$. This is obtained by the fairly straightforward computation (3.48), though the history term $Y_3(t) = \int_0^t V(s)\,\mathrm{d}s$ must be tracked in time. The second component of the density advection, $\boldsymbol{w}$, is found by numerically computing the convolution (3.39). Thus, the shape of the interface at each time iteration determines the domain of integration not only for $\boldsymbol{w}$ but also for the formulation of the force on the sphere (3.41). All velocity plots presented here are indicating the magnitude of the sphere's velocity.
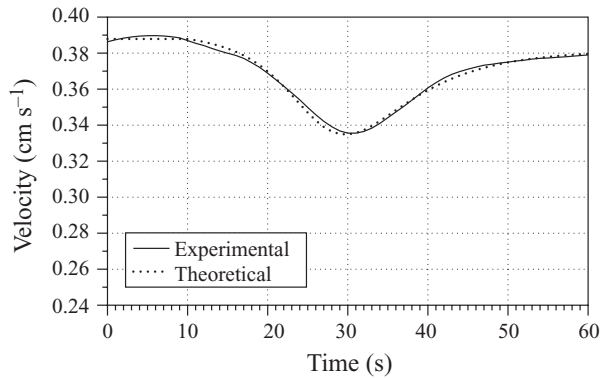
FIGURE 6. Sphere velocity comparisons from the experimental data and theoretical prediction for experimental parameters matching those in figure 3.
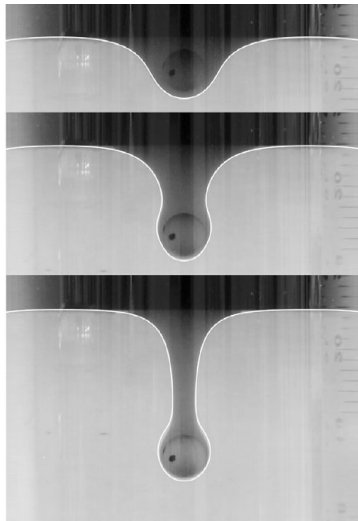

FIGURE 7. The computed, theoretical interface in white overlaid upon images of a sphere falling through stratified fluid with upper layer dyed for the same experimental parameters as in figure 2.

4.2. *Comparison with experimental results*

Once all the experimental parameters are determined through (accurate) measurements (i.e. viscosity and densities of the fluids, initial position and velocity of the sphere, size of the sphere and cylinder, etc.), we can directly compare the experimental data with numerical simulations. In figure 6, we see good agreement between the theoretically computed velocity profile and the data. Additionally, with the data from the experiment in figure 2, we can track the interface between the two fluids, and the comparison with the computed interface is shown in figure 7. It is also interesting to consider the effects on the interface evolution caused by neglecting the velocity or force arising from the buoyant fluid in our model. Comparison of the resulting approximations with experimental data are discussed in Camassa *et al.* (2009).

Next, we have explored experimentally a parametric range determined by varying sphere sizes and velocities. In figure 8(*a*), the maximum terminal velocity is an order of magnitude smaller than the previously shown experiment. Figure 8(*b*) shows data
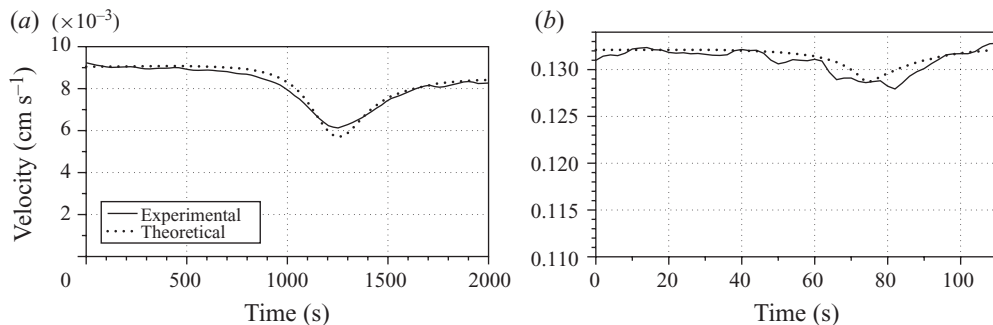
FIGURE 8. Theoretical and experimental velocity graphs for (*a*) a glass sphere of radius 0.24 cm and density $1.4\,\mathrm{g\,ml}^{-1}$ settling through a stratification of $1.37484\,\mathrm{g\,ml}^{-1}$ and $1.37623\,\mathrm{g\,ml}^{-1}$ density fluids with an average viscosity of 3.4 Pa s and (*b*) a steel sphere of radius 0.04 cm and density $7.74\,\mathrm{g\,ml}^{-1}$ settling through a stratification of $1.37720\,\mathrm{g\,ml}^{-1}$ and $1.37932\,\mathrm{g\,ml}^{-1}$ density fluids with an average viscosity of approximately 1.65 Pa s in a tank of 9.45 cm radius.
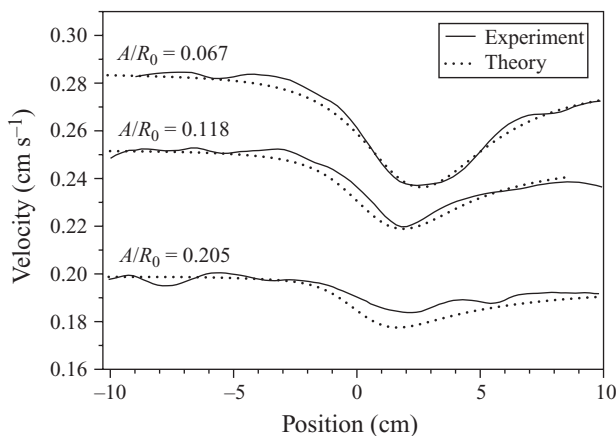
FIGURE 9. Theoretical and experimental velocity profiles for a 0.635 cm radius, $1.46755\,\mathrm{g\,ml}^{-1}$ sphere in a stratified fluid of densities $1.38362\,\mathrm{g\,ml}^{-1}$ and $1.38535\,\mathrm{g\,ml}^{-1}$ with viscosity ~ 2.2 Pa s in cylindrical tanks of radius 9.45 cm, 5.4 cm and 3.1 cm.

from an experiment in which the sphere size is an order of magnitude smaller than the previously shown comparisons and seems to have qualitative agreement with the theory. However, the spheres in this last data set are too small to be tracked without introducing large noise fluctuations, which make the comparison between theory and experiments difficult in such cases.

Additionally, we can model the effect of the tank walls on the sphere by using the same fluid stratification and varying the cylinder radius. The theoretical and experimental velocity graphs in figure 9 show that with decreasing ratio of sphere-to-cylinder radii, A/R_0, the accuracy of the asymptotic approximation, as expected, increases.

4.3. *Instantaneous points of zero velocity*

Points of zero (instantaneous) velocity can be visualized effectively by a plot of the instantaneous streamlines. Figure 10(*a*) shows the computed streamlines from the full theory (with the velocity in the lab frame). A streamline structure that includes fixed points of different (elliptic and hyperbolic) types and instantaneously closed orbits is
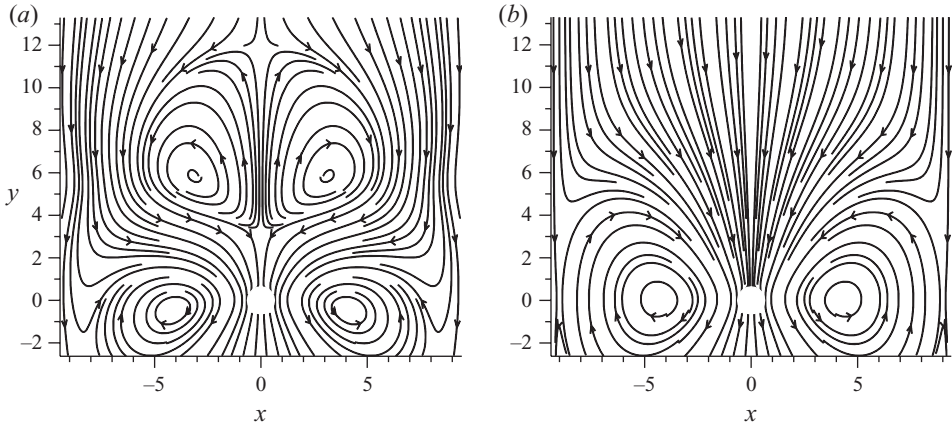
FIGURE 10. In the laboratory frame, the instantaneous streamlines for a sphere of radius 0.635 cm and density 1.5607 g ml^{-1} in a fluid of viscosity ~ 3.0 Pa s in a cylinder of radius 9.45 cm computed using the full theory with (*a*) fluid of top layer density 1.38147 g ml^{-1} and bottom layer density 1.38506 g ml^{-1} and (*b*) constant density.

clearly visible in this axial cross-section of the cylindrically symmetric flow. In this plot, the origin is shifted to coincide with the centre of the sphere, and the initial position of the interface is approximately 5.2 cm above the origin. The instantaneous hyperbolic stagnation points along the cylinder's axis, as well as the elliptic fixed points at the centre of the closed streamline pattern above the sphere (note that all these points change position in time), are solely due to the perturbation flow. (Fixed points off the vertical axis in these cross-sectional plots represent rings of points in the cylindrically symmetric flow where the velocity is instantaneously zero). In figure 10(*b*), we plot the calculated streamlines from the theory in *homogeneous* fluid: the instantaneous hyperbolic points of zero velocity above the sphere are absent. In the stratified case, the hyperbolic point immediately above the sphere marks the location where the upward motion of the fluid due to its buoyancy cancels the downward motion due to the moving sphere. A similar stagnation point was reported in the numerical results in Manga & Stone (1995), for the case of immiscible fluids.

Several remarks are in order. First, note that in these instantaneous streamline plots time should be considered as a parameter, whose variation leads to bifurcations of the velocity field. Thus, for instance, it can be expected that the two hyperbolic fixed points along the axis above the sphere emerge simultaneously with the elliptic fixed points and the connecting separatrix streamlines, in a bifurcation unfolding that leaves the total index fixed to zero for that cross-sectional region of the fluid domain, in agreement with the Poincaré index count for local bifurcations (see e.g. Ma & Wang 2001). Similarly, the magnitude of the density jump between the fluid layers can also be viewed as a bifurcation parameter. For large values of this parameter, it is plausible that a different bifurcation structure and unfolding takes place as time increases. While these bifurcation studies are interesting from a dynamical system perspective, they transcend the main focus of this paper, and we leave a more detailed analysis to future work.

Next, note that while figure 10(*b*) ought to represent the instantaneous streamlines due to a sphere falling in homogeneous fluid in a cylinder, we obtain them by using the *approximate* solution provided by Happel & Byrne (1954) along with our additional corrections, shown in (3.27) and (3.28). As discussed in § 3.7, a consistent asymptotic

approximation near the sphere requires the series $\boldsymbol{u}^{(1)} + (\boldsymbol{u}^{(2)} + \boldsymbol{u}^{(3)}) + \cdots$ (we neglect $\boldsymbol{u}^{(0)}$ since the streamlines are plotted in the lab frame) to be cutoff at the odd-labelled terms. Thus, the sum will satisfy the boundary conditions on the sphere, but not on the cylinder. Accordingly, the details of the instantaneous streamlines far from the sphere in figure 10 cannot be entirely correct, and end up magnifying a small error in the velocity field. For instance, the vertical velocity perturbation added in the truncation of the method of reflections, to correct for the fluid velocity on the sphere, generates a small flow far from the sphere which corresponds, in the streamline plots, to the appearance of open streamlines (particularly evident in the homogeneous case of figure 10(b) towards the top of the figure). This suggests a non-zero volume flux through horizontal planes far from the sphere. In calculating flux, we see that while $\boldsymbol{u}^{(2)}$ is subdominant to $\boldsymbol{u}^{(1)}$, the flux induced by $\boldsymbol{u}^{(1)} + \boldsymbol{u}^{(2)}$ is zero. This illustrates the non-uniformity in the asymptotic expansion of $\boldsymbol{u}$ using the method of reflections.

As shown from the model comparisons with experimental data in §4.2, the errors incurred in this approximation do not have significant dynamical effects on the sphere motion, at least for the parametric range we have focused on. We further tested the robustness of the approximation by exploring different ways to impose the boundary condition on the sphere, e.g. by imposing that if interface points touch the sphere they are assigned the sphere's velocity and hence move with the sphere; this had no noticeable effect on the sphere's dynamics nor the interface away from the sphere. This suggests that, as time progresses, the lower density fluid wrapping around the front of the sphere reaches thicknesses so small as to have no appreciable effects on the long time dynamics of the sphere, at least within the typical duration times of our experiments.

The dynamical effects of the interface morphology, as well as the diagnostic implications of the instantaneous streamline pattern with the appearance of fixed points in their phase portrait, are illustrated in figure 11. Figure 11(a–c) depicts displacements of the interface from its equilibrium position at three instants in time, labelled a, b, c and marked by vertical dashed lines across the sphere's velocity versus time plot in figure 11(d). As the figure demonstrates, the sphere attains its local minimum velocity well before the upper density fluid wraps fully around the sphere, which illustrates the need to accurately compute the interface shape to predict the extrema quantitatively. The 'neck' of the interface, corresponding to the vertical slope of the interface becoming a multi-valued function of the horizontal (radial) coordinate, develops when the sphere is accelerating towards its lower-fluid terminal velocity. The bifurcation in the streamline portrait leading to the appearance of the hyperbolic fixed points in the wake of the sphere can be first detected at the time $t \simeq 50\,\text{s}$, close to that of the minimum velocity, as shown by figure 11(e), which tracks the two hyperbolic fixed points' heights in time.

5. Approach to the interface

The perturbation stress (3.41) grows linearly with the density of the bottom layer fluid. In the limiting case where the bottom density tends to infinity, the stress force will also go to infinity and the sphere will come to rest before entering the lower layer of fluid. Thus, the behaviour of the sphere probably approaches that of a sphere falling towards a stationary interface of zero vertical velocity.

Two identical spheres approaching each other with equal, but opposite velocities will have zero vertical flow on the plane defined by the points equidistant from the two spheres. In free space, this construction has been solved by Happel & Brenner
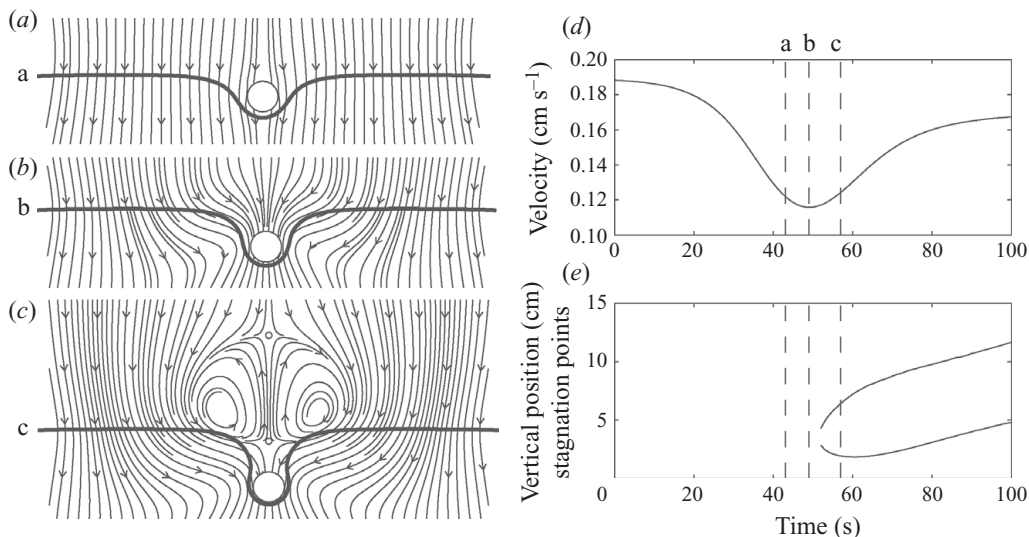
FIGURE 11. (*a–c*) Snapshots of the streamline portrait, interface position and stagnation point locations (indicated by small open circles) for a sphere of radius 0.635 cm and density 1.46755 g ml^{-1} in a stratified fluid of top layer density 1.37661 g ml^{-1} and lower layer density 1.38384 g ml^{-1}, with overall viscosity 3.62 Pa s, at three different instants in time. (*b*) Corresponds to time $t \simeq 48$ s at which the sphere's minimum velocity $V(t)$ is attained. (*d*) $V(t)$ plot – the dashed vertical lines mark the snapshot times of the streamline portraits (a, b, c) to the left. (*e*) Elevations of the two hyperbolic fixed points versus time in a moving frame of reference (with the sphere stationary) past the bifurcation at $t \simeq 50$ s.

(1965), who provide the formulation for the drag force

$$F_d = 6\pi A\mu V \left(1 + \frac{3}{4}\frac{A}{d} + \frac{9}{16}\left(\frac{A}{d}\right)^2 + \frac{19}{32}\left(\frac{A}{d}\right)^3 + \frac{3}{8}\left(\frac{A}{d}\right)^4 + \cdots\right), \qquad (5.1)$$

where d is half the distance between the centres of the spheres.

To visualize this limiting case, we show in figure 12 the velocity graphs of a sphere as formulated by our full theory with increasing bottom fluid density, keeping all other parameters the same. Solution (5.1) is obtained for the ideal free-space case. Hence, for the purpose of this visualization, we need to minimize the cylinder wall effects in our full theory. We pick the sphere to cylinder radius ratio $A/R_0 = 1/60$. This ratio, based on the study presented in §6, is sufficient to guarantee that the cylinder-wall boundary condition does not affect the model solution significantly, for most of the range of increasing density jumps we consider in figure 12. As the difference in the density of the sphere and the bottom fluid $\rho_s - \rho_2$ decreases, we see that the velocity profile approaches that of a sphere moving towards an interface with zero vertical velocity, plotted in solid black.

We use this limiting case to estimate the time scale T for our experiments. To leading order, the equation of motion for a sphere approaching a plane of zero vertical velocity in free space (Happel & Brenner 1965) is

$$m_s \frac{\mathrm{d}V}{\mathrm{d}t} = m_s g - m_f g - 6\pi A\mu V(t)\left(1 + \frac{3}{4}\frac{A}{H - Y_3(t)}\right), \qquad (5.2)$$

where H is the initial distance from the centre of the sphere to the interface and m_f is the mass of upper fluid displaced by the sphere. If we again neglect the time
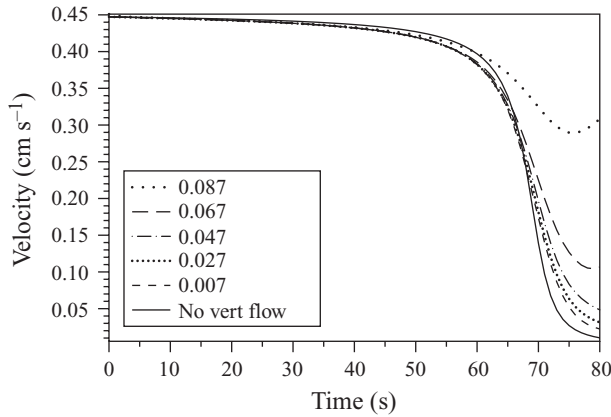
FIGURE 12. Velocity versus time graphs for a sphere of radius 0.635 cm and density 1.46755 g ml^{-1} initiated 30 cm from the interface separating a top fluid density 1.37661 g ml^{-1}, viscosity 1.76 Pa s, and changing bottom fluid density. The $\rho_s - \rho_2$ values decrease from 0.087 to 0.007 g ml^{-1} and the velocity graph approaches that of a sphere approaching an interface with zero vertical velocity, shown as a solid line, i.e. the solution of (5.2).

derivative, we can solve the resulting first order ordinary differential equation (ODE) for $Y_3(t)$ implicitly

$$t = \frac{6\pi A\mu}{(m_s - m_f)g} \left(Y_3(t) - \frac{3}{4}A \log \left(1 - \frac{Y_3(t)}{H} \right) \right), \tag{5.3}$$

while enforcing the initial condition that $Y_3(0) = 0$. A time scale for a sphere approaching a plane of zero vertical velocity can be defined by taking the difference between the times when the sphere exhibits a 10 % departure from terminal velocity to a 90 % departure (since the sphere comes to a stop at the interface, there is no lower layer terminal velocity). The velocities at these times are as follows:

$$V_{10\%} = 0.9 \times \frac{2}{9} \frac{A^2 g(\rho_s - \rho_1)}{\mu}, \tag{5.4}$$

$$V_{90\%} = 0.1 \times \frac{2}{9} \frac{A^2 g(\rho_s - \rho_1)}{\mu}. \tag{5.5}$$

Evaluating the equation for the position of the sphere versus $V(t)$,

$$Y_3(t) = -\frac{3A}{4} \left(\frac{(m_s - m_f)g}{6\pi A\mu V(t)} - 1 \right)^{-1} + H, \tag{5.6}$$

at these critical velocities yields the associated positions, which, once inserted into (5.3), provide the time scale

$$T = \frac{3}{4} \frac{\mu \, (40 + 9\log 9)}{Ag(\rho_s - \rho_1)}. \tag{5.7}$$

We can visualize this time scale on a velocity plot, where the region of interest is from 10 % deceleration from terminal velocity to 90 % towards the minimum velocity attained. In figure 13, the solid velocity curve is computed using the full theory for a density difference between the sphere and bottom fluid of 0.087 g ml^{-1}. The dashed plot is the velocity obtained from a sphere approaching an interface with zero vertical flow using the same parameters as in the stratified case. The respective
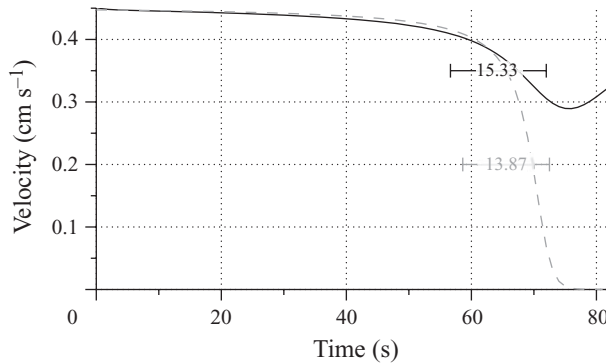
FIGURE 13. The time scales for a sphere in stratified fluid, in black, and a sphere approaching an interface of zero vertical velocity (which is reminiscent of the Tanner study with a rigid bottom), in grey, show that the time scale computed from (5.7) provides an estimate for the deceleration time interval (same parameters as in figure 12).

time scales and regions of deceleration are shown, and indicate that the zero vertical flow simplification will underestimate the time scale, thus overestimating the Strouhal number. Since our theory assumes that St is not large, an upper bound is appropriate.

Note that this calculation can be repeated for the case when the interfacial plane is replaced by a rigid wall, in which case the *horizontal* velocity components would also have to vanish. The leading-order coefficient would then change from 3/4 to 9/8, and would propagate through to the time scale formulation (5.7). As the stratified fluid would allow a horizontal velocity along the interface, the rigid wall approximation should provide an upper bound for the time scale of slowdown.

6. Non-dimensional trends

It may be of practical interest to explore trends resulting from parameter variations. Given the model's good agreement with the experimental data, and its derivation from first-principle physics, it can be used as a predictive tool within its range of validity. We can therefore explore parameters that will maximize the slowdown due to stratification. Such trends will also provide an *a priori* intuition of the sphere's behaviour when immersed in continuously stratified fluid. Note that these studies could run into regimes where finite Re effects become important, such as the Oseen far-field correction beyond the length scale $R \simeq A/Re$, where our theory can be expected to break down.

With the time scale for deceleration estimated in (5.7), we can compute the Strouhal number

$$St = \frac{6K(A/R_0)}{40 + 9\log 9}\left(1 + \frac{1}{2}\frac{\Delta\rho/\rho_{ref}}{\rho_s/\rho_{ref} - 1}\right). \tag{6.1}$$

The non-dimensionalized model,

$$\tilde{V} = \frac{Re}{6Fr^2}K(A/R_0)^{-1}\left(\frac{4\rho_s}{3\rho_{ref}} - \int_{-1}^{1}(1 - \tilde{z}^2)\tilde{\rho}_0(\tilde{z})\,d\tilde{z}\right.$$
$$\left. + \frac{\Delta\rho}{\pi\rho_{ref}}\int_{\tilde{\Omega}}\frac{1}{4}\left(\frac{3(\tilde{R}^2 + 2\tilde{Z}^2)}{\sqrt{\tilde{R}^2 + \tilde{Z}^2}^3} + \frac{\tilde{R}^2 - 2\tilde{Z}^2}{\sqrt{\tilde{R}^2 + \tilde{Z}^2}^5}\right)d\tilde{\Omega}\right), \tag{6.2}$$

$$St\frac{\partial\tilde{\rho}}{\partial\tilde{t}} + \left(\tilde{u} + \frac{Re}{Fr^2}\tilde{w}\right)\cdot\tilde{\nabla}\tilde{\rho} = 0, \tag{6.3}$$
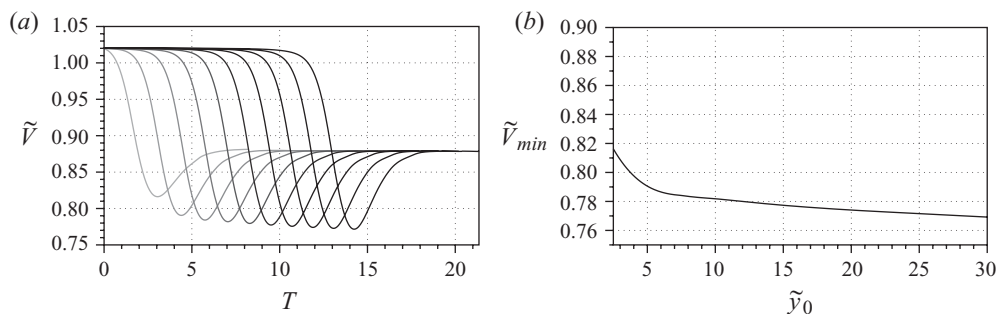
FIGURE 14. (*a*) The sphere velocity graphs for initial non-dimensional distance $\tilde{y}_0$ between the sphere and the interface increasing from 2.5 (grey) to 25 (black). (*b*) A plot of the minimum velocity with changing $\tilde{y}_0$ shows the slowdown increases with distance.
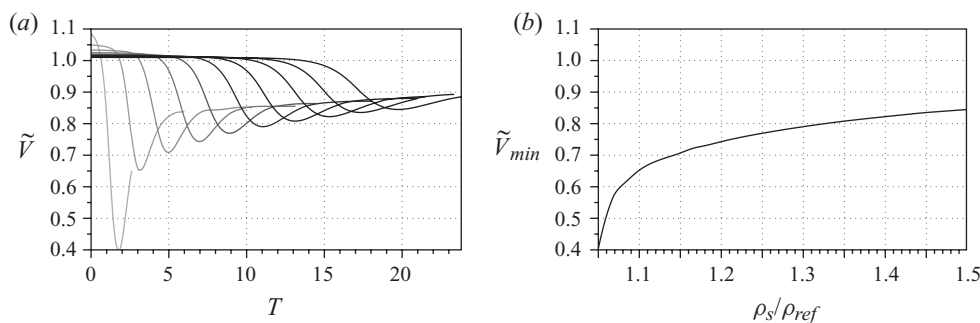

FIGURE 15. (*a*) The sphere velocity graphs for non-dimensionalized sphere velocity ρ_s/ρ_{ref} changing from 1.05 (grey) to 1.5 (black). (*b*) A plot of the minimum velocity as a function of ρ_s/ρ_{ref} shows the minimum velocity attained increases with the sphere density.

$$\tilde{\boldsymbol{w}} = \frac{\Delta\rho}{\rho_{ref}} \int_{\tilde{\Omega}} \tilde{\boldsymbol{W}} \, \mathrm{d}\tilde{\Omega}, \tag{6.4}$$

can be completely characterized by the following four parameters: $\tilde{y}_0$, ρ_s/ρ_{ref}, $\Delta\rho/\rho_{ref}$ and Re/Fr^2, therefore reducing the original seven parameter space, y_0, A, R_0, μ, ρ_1, ρ_2 and ρ_s. For the parameter studies below, the nominal values, $\tilde{y}_0 = 10$, $\rho_s/\rho_{ref} = 1.1$, $\Delta\rho/\rho_{ref} = 0.01$ and $Re/Fr^2 = 75$, are held fixed unless otherwise specified.

In figure 14, the initial distance of the interface to a sphere located at the origin changes from $\tilde{y}_0 = -2.5$ in grey to $\tilde{y}_0 = -25$ in black in increments of 2.5. The minimum velocity attained is higher when the interface is initiated closer to the sphere, as less deformation occurs and less buoyant fluid is entrained.

In figure 15, the sphere density is increasing from 1.05 (grey) to 1.5 (black) relative to the average fluid density. As the sphere increases in mass and effectively 'tunnels' through the stratification, the force resulting from the density deformation becomes less important. We see this reflected in the trends, where the minimum velocity attained increases with ρ_s/ρ_{ref}.

In figure 16(*a*), the density difference between the top and bottom layer is increasing from 0.002 (grey) to 0.02 (black) in increments of 0.002 relative to the average density of the fluid system. The density difference directly affects the density anomaly force and will enhance the slowdown of the sphere. Figure 16(*b*) shows the slowdown of the sphere to be more pronounced with increasing $\Delta\rho/\rho_{ref}$.
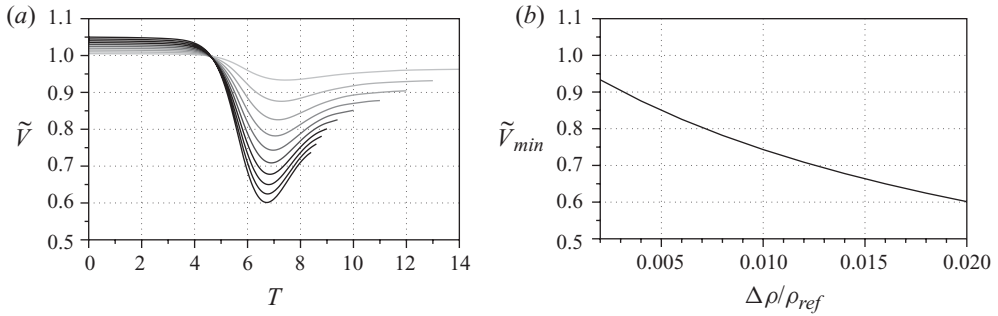
(*a*)

(*b*)

FIGURE 16. (*a*) The sphere velocity graphs for non-dimensionalized fluid density jump $\Delta\rho/\rho_{ref}$ changing from 0.002 (grey) to 0.02 (black). (*b*) A plot of the minimum velocity as a function of $\Delta\rho/\rho_{ref}$ shows the slowdown is amplified with increasing density jump.
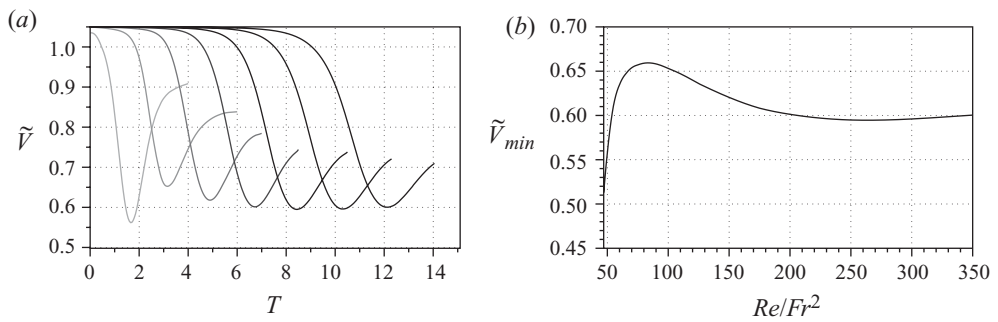
(*a*)

(*b*)

FIGURE 17. (*a*) The sphere velocity graphs for non-dimensionalized parameter Re/Fr^2 changing from 47 (grey) to 350 (black). (*b*) A plot of the minimum velocity as a function of Re/Fr^2 has a non-montonic trend.

In figure 17, Re/Fr^2 changes from 46 (in grey) to 350 (in black) by uneven increasing intervals. As this non-dimensional term multiplies as an overall coefficient both the homogeneous Stokes and the density induced perturbation velocity, and also determines the ratio A/R_0, it is unclear what the effects of its variations are on the sphere's motion. The trend of the minimum velocity attained appears to be non-monotonic. Note that in varying Re/Fr^2 we are changing the ratio of gravitational to viscous forces. With the exception of this parameter, which can be viewed as a drag coefficient, all the trends have intuitive effects on the behaviour of the falling sphere.

While the previous figures document the behaviour arising for certain cross-sections through the four-dimensional parametric space, a particular cross-section worth focusing on concerns the effects of varying A/R_0. We show in figure 18 the results from the theoretical model when increasing the inverted ratio R_0/A from 40 in grey to 200 in black. At these scales, where both the Tanner and the far-field Oseen length scales become important, the density effects of the present model are nonetheless singled out. In particular, this study gives some information on the mathematically relevant question of whether a well defined, physically acceptable free-space limit of our theory (solely based on the Stokes approximation) exists due to the presence of stratification. This is in contrast to the homogeneous fluid counterpart, where the free-space limit leads to well known divergences, such as that of the volume of fluid dragged by the moving sphere, which need to be corrected with the Oseen asymptotic contribution of the inertia terms in the Navier–Stokes equations.
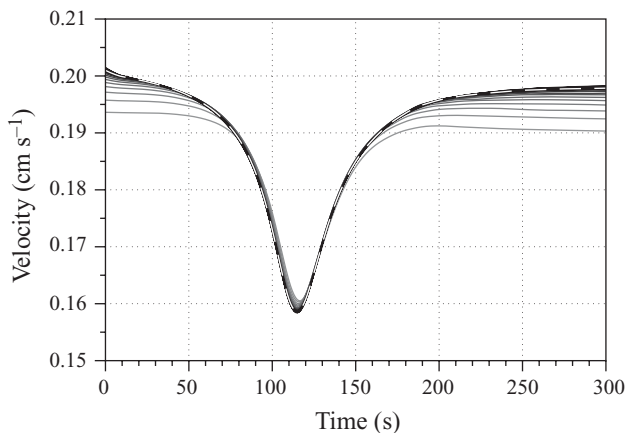
FIGURE 18. Velocity plots for R_0/A increasing from 40 (in grey) to 200 (in black) in increments of 10 for a sphere falling through stratified fluid. The sphere is initiated at a distance $y_0/A = 40$ away from the interface, within the Tanner length scale. The velocity curve marking the transition through the non-dimensionalized Oseen length scale of $1/Re = 146$ is shown as a dashed curve.

For the results depicted in figure 18, the sphere is initialized at a distance of $y_0/A = 40$, so as the cylinder radius increases, the effects of the interface on the velocity of the sphere will be reflected by a more immediate initial slowdown indicating that a terminal velocity may not be achieved in the upper fluid. When R_0/A increases beyond the Oseen length scale of A/Re, this transition is marked in figure 18 as the dashed curve. Since the velocity plots appear to be converging as R_0/A increases, it seems that a physically acceptable free-space limit may exist even in the absence of an Oseen inertial correction. We remark that this conclusion hinges on the good convergence exhibited by the model up to intermediate time scales (up to 150 s in this figure). Further improvements on the model are needed to capture long-time trends correctly, particularly at either small or large R_0/A ratios. Small errors in the asymptotic approximations of the boundary conditions discussed in §4.3 do in fact accumulate over long times and prevent the model dynamics from maintaining the terminal velocity force-balance on long time scales. This may account for the appearance of a relative maximum in the velocity plot, noticeable for the smaller R_0/A ratios of figure 18. The existence of a relative maximum would imply an overshoot above the terminal velocity of the lower fluid, an additional feature with respect to the monotonic increase to this limiting value after the minimum velocity slowdown seen in most computations over intermediate time scales.

7. Comparison with other models

In §7, we compare our results with that of two simple models, which could be viewed as intuitive starting points in a straightforward generalization to the stratified case of what is known for the case of homogenous fluids. However, as we will see, these models fail to represent our experimental data, indicating that our full model (3.48) may actually be the minimum required in the experimental range of parameters we have explored.

7.1. *Archimedean model*

Possibly the simplest way to account for the higher-density lower fluid is to calculate the volume of entrained fluid and directly apply its Archimedean buoyant force to the
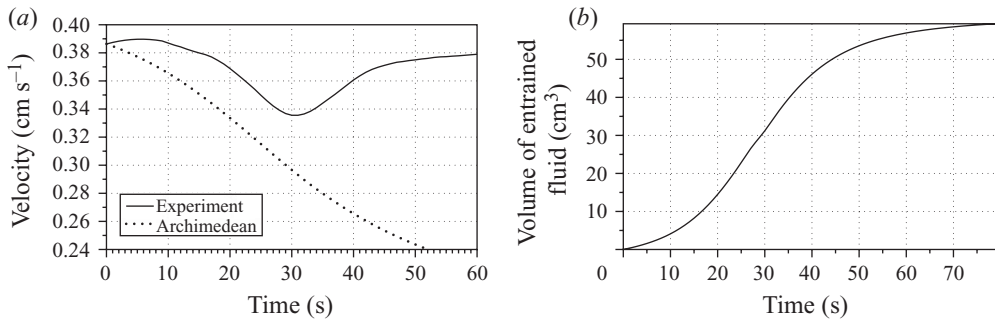
FIGURE 19. Using an Archimedean model, (*a*) we compare the computed velocity profile and the experimental data, and find that the velocity profile is monotonically decreasing due to a (*b*) monotonically increasing volume of entrained fluid.

sphere. In this case, our equations of motion for the sphere and fluid in the moving frame of reference would become

$$m_s \frac{\mathrm{d}V(t)}{\mathrm{d}t} = m_s g - g \int_{\Omega_s} \rho_0(x_3 + Y_3(t)) \,\mathrm{d}\Omega_s - 6\pi A \mu V(t) K$$

$$+ g \int_{\Omega_f} (\rho(\boldsymbol{x}, t) - \rho_0(x_3 + Y_3(t))) \,\mathrm{d}\Omega_f, \tag{7.1}$$

$$\frac{\partial \rho}{\partial t}(\boldsymbol{x}, t) + \boldsymbol{u}(\boldsymbol{x}, t) \cdot \nabla \rho(\boldsymbol{x}, t) = 0, \tag{7.2}$$

where $K = (1 - 2.10444(A/R_0) + 2.08877(A/R_0)^3 + \cdots)^{-1}$ is again the extra coefficient for a Stokes drag in a pipe and Ω_f is the volume of entrained fluid.

The numerical simulation of this model uses the approximation for $\boldsymbol{u}(\boldsymbol{x}, t)$ given in §3.2 with parameters matching those in figure 3. The resulting velocity profile in figure 19(*a*) is monotonically decreasing, due to the monotonically increasing volume of entrained fluid, shown in figure 19(*b*). We remark, however, that drift volume computations in cylinders are affected by the truncation approximation when using the method of reflections. Also note that because this simplistic Archimedean model does not take into account the buoyancy of the fluid in the advection equation, the velocity of the sphere is unable to approach the terminal velocity of the bottom layer after slowing down, even if the entrained volume were to reach a finite limit. Additionally, this model does not account for the location of the entrained fluid relative to the sphere. Hence, buoyant fluid at large distances from the sphere has a significant effect on the system, and the centre of mass of the sphere with entrained fluid may migrate outside of the sphere boundary. The Archimedean buoyancy force calculated in this model is therefore an *upper bound* to the buoyant force of the entrained fluid.

7.2. *Modified Maxey–Riley model*

Maxey & Riley (1983) provided a solution for the unsteady motion of a sphere in a non-uniform flow. For the fluid velocity, the time derivative in the inertial term is retained, corresponding to scalings for which the Strouhal number might be large while keeping the Reynolds number small, and gives rise to the well-known Basset history term in the final model. As a point of comparison, we modify this equation of motion with a variable fluid density and zero ambient flow,
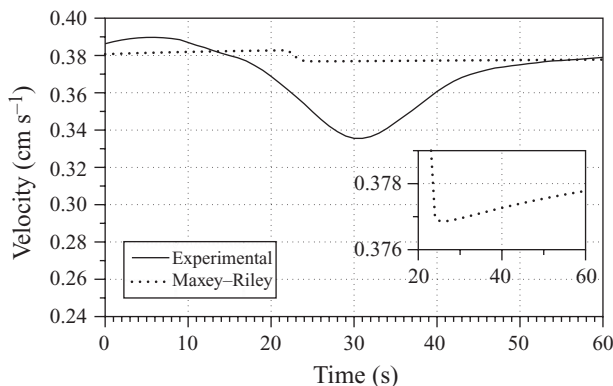
FIGURE 20. Velocity profile computed from the modified Maxey–Riley model overlaid upon the experimental data.

$$m_s \frac{\mathrm{d}V(t)}{\mathrm{d}t} = (m_s - m_f)g - \frac{1}{2} m_f \frac{\mathrm{d}V(t)}{\mathrm{d}t} - 6\pi A \mu V(t)$$
$$- 6\pi A^2 \mu \int_0^t \frac{\mathrm{d}V(\tau)}{\mathrm{d}\tau} \left(\pi \nu (t - \tau)\right)^{-1/2} \mathrm{d}\tau, \quad (7.3)$$

where

$$m_f = \int_{\Omega_s} \rho(x_3 + Y_3(t)) \, \mathrm{d}\Omega_s. \quad (7.4)$$

Again, we can compute the velocity predicted by this model using parameters from the experiment in figure 3. The results are shown in figure 20. It is interesting to note that the computed velocity profile appears monotonic, but as the inset reveals, it can in fact present a slight dip in the velocity. This model does not account for the deformation of the density field, and can only be justified under the assumption that the sphere sees only the unperturbed background density distribution. Thus, the time scale for the sphere falling through the density transition must be shorter than the diffusion scale for the fluid, but longer than the time scale for the displaced fluid to diffuse back to its original background stratification values. The phenomenon of enhanced diffusion in regions of high shear flows, mentioned in §3, could in principle make such disparity of time scales possible, however this regime has yet to be pinpointed with our experimental parameters. We remark that in the case of an infinite *linear* stratification, for which the background stratification remains constant in time, this model could apply under sufficiently large diffusivities.

8. Discussion

Our study of a sphere falling through fluid with (sharp) density stratifications shows a significant slowdown beyond the terminal velocity of the bottom denser fluid when the sphere approaches the region of high stratification. The full theoretical model (3.42) and (3.43) we have derived from first principles shows good agreement with the experimental data and has no adjustable parameters. While it does not lead to a closed form solution, the numerical integration needed for its solution is limited to a standard ODE code for the Lagrangian advection of the interface. This allows a fast and accurate solution of the stratified fluid motion fully coupled to the rigid body (sphere) dynamics through its moving boundary.

From a mathematical perspective, it is interesting to consider the theoretical model we have developed in the case of free space, which eliminates the approximations needed to enforce the no-slip boundary condition on the cylinder wall, thereby making the model exact for flows in the Stokes regimes. However, as is well known, the slow decay at infinity of the velocity field induced by the moving sphere in the Stokes approximation leads to divergences of integral quantities, giving rise to inconsistencies of the free-space theory for homogeneous fluids sometimes collectively referred to as 'Stokes paradox'. This affects our theory as well, since integrals such as those in the Oseen's Green's function convolution lose their convergence in the free-space limit. However, it can be shown that infinite divergences due to the slow decay at infinity of the interface displacement occur with opposite sign in the force balance, suggesting that a regularization by cancellation of infinities could occur in the *stratified* infinite case. Of course, the far-field fluid's inertia is the ultimate physical origin of the regularization of Stokes paradox divergences, which effectively cuts off the domain of integration at the Oseen's length scale A/Re, but the regularization by sharp stratification suggested by our model could effectively introduce a cutoff at shorter range for large enough density jumps. Another noteworthy generalization of our theory for sharp density stratification is to approximate a broader range of stratifications by 'experimental discretization' through multi-layer density profiles. In particular, we are now considering both experimentally and analytically density 'staircases' approximating a linear density profile, as studied by Yick *et al.* (2009). We expect that the dynamics of a sphere falling through a staircase stratification would oscillate around a mean, which could be related to a linear stratification profile, thereby providing direct comparison with the results of Yick *et al.* (2009). Finally, a promising avenue of investigation is that of higher, but still moderate, Reynolds number situations, which can easily be achieved experimentally when working with corn syrup by increasing its water content. This regime should bring forth other important effects such as the dynamical role played by internal gravity waves and the nature of the overshoot of the entrained fluid as it returns to equilibrium (Lin 2009). These will be the focus of a future publication.

Appendix A. Internal gravity waves in a two-fluid system

Consider a two-fluid system of density ρ_1 and velocity $\boldsymbol{u}^{(1)}$ upper layer and density ρ_2 and velocity $\boldsymbol{u}^{(2)}$ lower layer. Let x and z indicate the horizontal and vertical directions, respectively. We have the following equations of motion:

$$\boldsymbol{u}_t^{(j)} = \nu_j \Delta \boldsymbol{u}^{(j)} - 1/\rho_j \nabla p^{(j)}, \tag{A 1}$$

$$\nabla \cdot \boldsymbol{u}^{(j)} = 0, \tag{A 2}$$

for $j = 1, 2$. Assuming

$$u^{(j)} = g_j(z) \mathrm{e}^{-\mathrm{i}\omega t + \mathrm{i}kx}, \tag{A 3}$$

$$v^{(j)} = h_j(z) \mathrm{e}^{-\mathrm{i}\omega t + \mathrm{i}kx}, \tag{A 4}$$

and assuming that $\boldsymbol{u}^{(1)} \to 0$ as $z \to \infty$ and $\boldsymbol{u}^{(2)} \to 0$ as $z \to -\infty$, we have the following solutions:

$$u^{(1)} = \mathrm{e}^{\mathrm{i}kx - \mathrm{i}t\omega}(A_1 \mathrm{e}^{-kz} + B_1 \mathrm{e}^{-m_1 z}), \tag{A 5}$$

$$v^{(1)} = \mathrm{e}^{\mathrm{i}kx - \mathrm{i}t\omega}\left(\mathrm{i}A_1 \mathrm{e}^{-kz} + \frac{\mathrm{i}k}{m_1}B_1 \mathrm{e}^{-m_1 z}\right), \tag{A 6}$$

$$p^{(1)} = \rho_1 \left(\frac{\omega}{k}A_1 \mathrm{e}^{\mathrm{i}kx - kz - \mathrm{i}t\omega} - gz\right), \tag{A 7}$$

$$u^{(2)} = \mathrm{e}^{\mathrm{i}kx - \mathrm{i}t\omega}(A_2 \mathrm{e}^{kz} + B_2 \mathrm{e}^{m_2 z}), \tag{A 8}$$

$$v^{(2)} = \mathrm{e}^{\mathrm{i}kx - \mathrm{i}t\omega}\left(-\mathrm{i}A_2 \mathrm{e}^{kz} - \frac{\mathrm{i}k}{m_2}B_2 \mathrm{e}^{m_2 z}\right), \tag{A 9}$$

$$p^{(2)} = \rho_2 \left(\frac{\omega}{k}A_2 \mathrm{e}^{\mathrm{i}kx + kz - \mathrm{i}t\omega} - gz\right), \tag{A 10}$$

where $m_j = \sqrt{k^2 - \mathrm{i}\omega/\nu_j}$. Matching velocities and stresses at the interface, we have the following dispersion relation:

$$\omega m_1 m_2 \left(k(\rho_1 - \rho_2)^2 \omega^2 - (\rho_1 + \rho_2)(m_2 \rho_1 + \rho_2 m_1)\omega^2 \right.$$
$$\left. + gk(\rho_1 - \rho_2)(-m_2 \rho_1 + k(\rho_1 + \rho_2) - \rho_2 m_1)\right) = 0. \tag{A 11}$$

Assuming limiting case $2\mu k^2/(\rho_1 + \rho_2) \ll \sqrt{gk}$, we retrieve the root

$$\omega = \pm\sqrt{\frac{gk(\rho_2 - \rho_1)}{\rho_1 + \rho_2}} + \frac{\sqrt{2\mu}\rho_1 \rho_2 (\mp 1 - \mathrm{i})}{\sqrt{\rho_2}\rho_1 + \rho_2 \sqrt{\rho_1}}\left(\frac{gk^5(\rho_2 - \rho_1)}{\rho_1 + \rho_2}\right)^{1/4} - \frac{2\mathrm{i}k^2 \mu \left(\rho_1^2 + \rho_2^2\right)}{\left(\sqrt{\rho_1} + \sqrt{\rho_2}\right)^2 (\rho_1 + \rho_2)^2}. \tag{A 12}$$

On the other hand, assuming the very viscous limit of $2\mu k^2/(\rho_1 + \rho_2) \gg \sqrt{gk}$, we get three negative roots (since in a stable stratification $\rho_2 > \rho_1$), all of which are purely imaginary:

$$\omega = -\frac{\mathrm{i}k^2 \mu}{\rho_1}, \quad -\frac{\mathrm{i}k^2 \mu}{\rho_2}, \quad -\frac{\mathrm{i}g(\rho_2 - \rho_1)}{4\mu k}. \tag{A 13}$$

This limit corresponds to wavenumber $k \gg (g(\rho_1 + \rho_2)^2/4\mu^2)^{1/3}$, which for our experimental parameters are in the regime of wavelengths $\lambda \ll 30\,\mathrm{cm}$ (using the reduced gravity of $g' = 2g(\rho_2 - \rho_1)/(\rho_1 + \rho_2)$). Thus, for our container dimensions, all internal waves are overdamped.

Appendix B. Stokes flow past a sphere in a cylinder

The asymptotic expansion for $\boldsymbol{u} = \boldsymbol{u}^{(0)} + \boldsymbol{u}^{(1)} + \cdots$, as formulated in Happel & Byrne (1954) in cylindrical coordinate (R, θ, Z) with $r = \sqrt{R^2 + Z^2}$ is

$$u_Z^{(0)} = -V(t)\left[\frac{-3A}{4r} - \frac{3AZ^2}{4r^3} - \frac{A^3}{4r^3} + \frac{3Z^2 A^3}{4r^5}\right], \tag{B 1}$$

$$u_R^{(0)} = -V(t)\left[\frac{-3ARZ}{4r^3} + \frac{3A^3 RZ}{4r^5}\right], \tag{B 2}$$

$$u_Z^{(1)} = \frac{1}{2\pi}\int_0^\infty \hat{u}_Z(R, \lambda)\cos(\lambda Z)\,\mathrm{d}\lambda, \tag{B 3}$$

$$u_R^{(1)} = \frac{1}{2\pi} \int_0^\infty \hat{u}_R(R, \lambda) \sin(\lambda Z) \, d\lambda, \tag{B 4}$$

$$\frac{P^{(2)}}{\mu} = \frac{1}{2\pi} \int_0^\infty \hat{P}(R, \lambda) \sin(\lambda Z) \, d\lambda, \tag{B 5}$$

where

$$\hat{u}_Z(R, \lambda) = \frac{\lambda R}{2}(H(\lambda) + G(\lambda))I_1(\lambda R) + H(\lambda)I_0(\lambda R), \tag{B 6}$$

$$\hat{u}_R(R, \lambda) = \frac{\lambda R}{2}(H(\lambda) + G(\lambda))I_0(\lambda R) - G(\lambda)I_1(\lambda R), \tag{B 7}$$

$$\hat{P}(R, \lambda) = \lambda(H(\lambda) + G(\lambda))I_0(\lambda R), \tag{B 8}$$

$$\hat{u}_Z(R, \lambda) = \frac{\lambda R}{2}(H(\lambda) + G(\lambda))I_1(\lambda R) + H(\lambda)I_0(\lambda R), \tag{B 9}$$

$$\hat{u}_R(R, \lambda) = \frac{\lambda R}{2}(H(\lambda) + G(\lambda))I_0(\lambda R) - G(\lambda)I_1(\lambda R), \tag{B 10}$$

and

$$H(\lambda) = \frac{AV\left\{3 - \left(6 + \frac{A^2}{R_0^2}\alpha^2\right)(K_0(\alpha)I_2(\alpha) + K_1(\alpha)I_1(\alpha))\right\}}{I_0(\alpha)I_2(\alpha) - I_1(\alpha)^2}, \tag{B 11}$$

$$G(\lambda) = \frac{AV\left\{-3 + \frac{A^2}{R_0^2}\alpha^2(K_1(\alpha)I_1(\alpha) + K_2(\alpha)I_0(\alpha))\right\}}{I_0(\alpha)I_2(\alpha) - I_1(\alpha)^2}, \tag{B 12}$$

where I_j and K_j are modified Bessel functions of the first and second kind.

Appendix C. Perturbation velocity

The perturbation velocity is written as a convolution with the Green's function $W_j(\boldsymbol{x}, \boldsymbol{y})$,

$$w_j^{(0)}(\boldsymbol{x}, t) = \int_{\Omega_f} \epsilon G(\boldsymbol{y}, t)W_j(\boldsymbol{x}, \boldsymbol{y}) \, d\Omega_f, \tag{C 1}$$

where the Green's function is written explicitly as $W_j(\boldsymbol{x}, \boldsymbol{y}) = gT_{j3}/8\pi\mu$ (Oseen 1927) and

$$T_{jk} = \frac{\delta_{jk}}{r} + \frac{(x_j - y_j)(x_k - y_k)}{r^3} - \frac{A}{|\boldsymbol{y}|}\frac{\delta_{jk}}{r^*} - \frac{A^3}{|\boldsymbol{y}|^3}\frac{(x_j - y_j^*)(x_k - y_k^*)}{r^{*3}}$$

$$- \frac{|\boldsymbol{y}|^2 - A^2}{|\boldsymbol{y}|}\left\{\frac{y_j^* y_k^*}{A^3 r^*} - \frac{A}{|\boldsymbol{y}|^2 r^{*3}}\left[y_j^*(x_k - y_k^*) + y_k^*(x_j - y_j^*)\right]\right.$$

$$\left. + \frac{2y_j^* y_k^*}{A^3}\frac{y_l^*(x_l - y_l^*)}{r^{*3}}\right\} - (|\boldsymbol{x}|^2 - A^2)\frac{\partial \phi_k}{\partial x_j}, \tag{C 2}$$

$$\phi_k = \frac{|\boldsymbol{y}|^2 - A^2}{2|\boldsymbol{y}|^3}\left(\frac{3y_k}{Ar^*} + \frac{A(x_k - y_k^*)}{r^{*3}} + \frac{2y_k}{A}y_j^*\frac{\partial}{\partial x_j}\frac{1}{r^*}\right.$$

$$\left. + \frac{3A}{|\boldsymbol{y}^*|}\frac{\partial}{\partial y_k^*}\log\frac{|\boldsymbol{y}^*|r^* + x_j y_j^* - |\boldsymbol{y}^*|^2}{|\boldsymbol{x}||\boldsymbol{y}^*| + x_j y_j^*}\right), \tag{C 3}$$

where $y^* = (A^2/|y|^2)y$, $r = |y - x|$, $r^* = |y^* - x|$, and the convention of sum over repeated indexes is used. Thus, the Green's function can be viewed as resulting from the superposition of appropriate singularities inside the radius A sphere at the reflection point corresponding to the position y of the Stokeslet outside the sphere (Higdon 1979). The pressure components of the Green's function corresponding to those of the velocity tensor $T_{jk}(x, y)$ are

$$P_k = 2\mu \left[\frac{x_k - y_k}{r^3} - \frac{A^3}{|y|^3} \frac{x_k - y_k^*}{r^{*3}} - \left(\phi_k + 2x_l \frac{\partial \phi_k}{\partial x_l} \right) \right]. \tag{C 4}$$

Appendix D. Force exerted on a rigid sphere by a Stokeslet in an infinite fluid

Using the general reciprocal theorem as stated by Happel & Brenner (1965), we can solve for the force on a sphere due to a Stokeslet in free space. Given the Stokes flow due to a sphere moving with velocity V in free space, we have the following system of equations:

$$\nabla \cdot \sigma = 0, \tag{D 1}$$
$$\nabla \cdot u_s = 0, \tag{D 2}$$
$$u_s = V \quad \text{on } \partial S, \tag{D 3}$$
$$u_s \to 0 \quad \text{as } |x| \to \infty, \tag{D 4}$$

where ∂S is the surface of the sphere, whose solution is well known. Next, we would like to solve the following system for the force on the sphere due to the perturbation flow w:

$$\nabla \cdot \sigma_w = \epsilon G(x, t)\rho_{ref}\hat{g}, \tag{D 5}$$
$$\nabla \cdot w = 0, \tag{D 6}$$
$$w = 0 \quad \text{on } \partial S, \tag{D 7}$$
$$w \to 0 \quad \text{as } |x| \to \infty. \tag{D 8}$$

Combining these two systems and using incompressibility results in the following system:

$$\nabla \cdot (u_s \cdot \sigma_w) = u_s \cdot \epsilon G(x, t)\rho_{ref}\hat{g}, \tag{D 9}$$
$$\nabla \cdot (w \cdot \sigma) = 0. \tag{D 10}$$

By subtracting these two equations and integrating over the fluid domain Ω_f (assuming the convergence of these integrals), we have

$$\int_{\Omega_f} \nabla \cdot (u_s \cdot \sigma_w) \, d\Omega_f - \int_{\Omega_f} \nabla \cdot (w \cdot \sigma) \, d\Omega_f = \int_{\Omega_f} u_s \cdot \epsilon G(x, t)\rho_{ref}\hat{g} \, d\Omega_f, \tag{D 11}$$

which, upon applying the divergence theorem to the left hand side of the equation, gives

$$\int_{\partial S} u_s \cdot \sigma_w \cdot \hat{n} \, dS - \int_{\partial S} w \cdot \sigma \cdot \hat{n} \, dS = \int_{\Omega_f} u_s \cdot \epsilon G(x, t)\rho_{ref}\hat{g} \, d\Omega_f. \tag{D 12}$$

Using the boundary conditions yields

$$\int_{\partial S} V \cdot \sigma_w \cdot \hat{n} \, dS = \int_{\Omega_f} u_s \cdot \epsilon G(x, t)\rho_{ref}\hat{g} \, d\Omega_f. \tag{D 13}$$

Considering only the vertical component of the force leads to the expression

$$\left(\int_{\partial S} \boldsymbol{\sigma}_w \cdot \hat{\boldsymbol{n}} \, \mathrm{d}S \right)_3 = \frac{\rho_{ref} g}{V_3} \int_{\Omega_f} \epsilon G(\boldsymbol{x}, t) u_{s3} \, \mathrm{d}\Omega$$

$$= \rho_{ref} g \int_{\Omega_f} \epsilon G(\boldsymbol{x}, t) \left(\frac{-3A}{4r} - \frac{3AZ^2}{4r^3} - \frac{A^3}{4r^3} + \frac{3Z^2 A^3}{4r^5} \right) \mathrm{d}\Omega_f$$

$$= \rho_{ref} g \int_{\Omega_f} \epsilon G(\boldsymbol{x}, t) \left(\frac{-3A(2Z^2 + R^2)}{4r^3} + \frac{A^3(2Z^2 - R^2)}{4r^5} \right) \mathrm{d}\Omega_f. \quad (\mathrm{D}\,14)$$

Thus, the force on a sphere due to the perturbation flow is

$$\left(\int_{\partial S} \boldsymbol{\sigma}_w \cdot \hat{\boldsymbol{n}} \, \mathrm{d}S \right)_3 = \rho_{ref} g \int_{\Omega_f} \epsilon G(\boldsymbol{x}, t) \left(\frac{-3A(2Z^2 + R^2)}{4r^3} + \frac{A^3(2Z^2 - R^2)}{4r^5} \right) \mathrm{d}\Omega_f. \quad (\mathrm{D}\,15)$$

REFERENCES

ABAID, N., ADALSTEINSSON, D., AGYAPONG, A. & MCLAUGHLIN, R. M. 2004 An internal splash: levitation of falling spheres in stratified fluids. *Phys. Fluids* **16** (5), 1567–1580.

AKERS, B. & BELMONTE, A. 2006 Impact dynamics of a solid sphere falling into a viscoelastic micellar fluid. *J. Non-Newtonian Fluid Mech.* **135**, 97–108.

BATCHELOR, G. K. 1967 *An Introduction to Fluid Dynamics*. Cambridge University Press.

BERCOVICI, D. & MAHONEY, J. 1994 Double flood basalts and plume head separation at the 660-kilometer discontinuity. *Science* **266**, 1367–1369.

BRENNER, H. 1961 The slow motion of a sphere through a viscous fluid towards a plane surface. *Chem. Engng Sci.* **16**, 242–251.

CAMASSA, R., FALCON, C., LIN, J., MCLAUGHLIN, R. M. & PARKER, R. 2009 Prolonged residence times for particles settling through stratified miscible fluids in the Stokes regime. *Phys. Fluids* **21**, 031702-1–4.

CAMASSA, R., MCLAUGHLIN, R. M., MOORE, M. & VAIDYA, A. 2008 Brachistochrone paths in potential and stokes flow past a sphere. *Phys. Lett.* A **372**, 6742–6749.

CONDIE, S. A. & BORMANS, M. 1997 The influence of density stratification on particle settling, dispersion and population growth. *J. Theor. Biol.* **187**, 65–75.

DARWIN, C. 1953 Note on hydrodynamics. *Proc. Camb. Phil. Soc.* **49**, 342–254.

DENMAN, K. L. & GARGETT, A. E. 1995 Biological–physical interactions in the upper ocean: the role of vertical and small scale transport processes. *Annu. Rev. Fluid Mech.* **27**, 225–255.

HAPPEL, J. & BRENNER, H. 1965 *Low Reynolds Number Hydrodynamics with Special Applications to Particulate Media*. Noordhoff International Publishing.

HAPPEL, J. & BYRNE, B. J. 1954 Motion of a sphere and fluid in a cylindrical tube. *Ind. Engng Chem.* **46** (6), 1181–1186.

HIGDON, J. J. L. 1979 A hydrodynamic analysis of flagellar propulsion. *J. Fluid Mech.* **90** (4), 685–711.

JURINE, D., JAUPART, C., BRANDEIS, G. & TACKLEY, P. J. 2005 Penetration of mantle plumes through depleted lithosphere. *J. Geophys. Res.* **110**, B10104.1–B10104.18.

KELLOGG, W. W. 1980 Aerosols and climate. In *Interaction of Energy and Climate* (ed. W. Bach, J. Prankrath & J. Williams), pp. 281–296. D. Reidel.

LIN, J. 2009 An experimental and mathematical study on the prolonged residence time of a sphere falling through stratified fluids at low Reynolds number. PhD thesis, University North Carolina, North Carolina, NC.

LINTON, C. M. 1995 Multipole methods for boundary-value problems involving a sphere in a tube. *IMA J. Appl. Maths* **55**, 187–204.

MA, T. & WANG, S. 2001 A generalized Poincaré–Hopf index formula and its applications to 2-D incompressible flows. *Nonlinear Anal. Real World Appl.* **2**, 467–482.

MacIntyre, S., Alldredge, A. L. & Gottschalk, C. C. 1995 Accumulation of marine snow at density discontinuities in the water column. *Limnol. Oceanogr.* **40** (3), 449–468.

Manga, M. & Stone, H. A. 1995 Low Reynolds number motion of bubbles, drops and rigid spheres through fluid–fluid interfaces. *J. Fluid Mech.* **287**, 279–298.

Maxey, M. R. & Riley, J. J. 1983 Equation of motion for a small rigid sphere in a non-uniform flow. *Phys. Fluids* **26** (4), 883–889.

Oseen, C. W. 1927 *Hydrodynamik*. Academische Verlagsgesellschaft M. B. H.

Parsons, J. D., Bush, J. W. M. & Syvitski, J. P. M. 2001 Hyperpycnal plume formation from riverine outflows with small sediment concentrations. *Sedimentology* **48**, 465–478.

Rard, J. A. & Miller, D. G. 1979 The mutual diffusion coefficients of NaCl–H_2O and $CaCl_2$–H_2O at 25°C from Rayleigh interferometry. *J. Sol. Chem.* **8**, 701–716.

Srdić-Mitrović, A. N., Mohamed, N. A. & Fernando, H. J. S. 1999 Gravitational settling of particles through density interfaces. *J. Fluid Mech.* **381**, 175–198.

Sutor, M. M. & Dagg, M. J. 2008 The effects of vertical sampling resolution on estimates of Plankton biomass and rate calculations in stratified water columns. *Estuar. Coast. Shelf Sci.* **78**, 107–121.

Tanner, R. I. 1963 End effects in falling-ball viscometry. *J. Fluid Mech.* **17**, 161–170.

Taylor, G. 1953 Dispersion of soluble matter in solvent flowing slowly through a tube. *Proc. R. Soc. Lond.* A **219**, 186–203.

Turco, R. P., Toon, O. B., Ackerman, T. P., Pollack, J. B. & Sagan, C. 1990 Climate and smoke: an appraisal of nuclear winter. *Science* **247** (4939), 662–665.

Widder, E. A., Johnsen, S., Bernstein, S. A., Case, J. F. & Neilson, D. J. 1999 Thin layers of bioluminescent copepods found at density discontinuities in the water column. *Mar. Biol.* **134**, 429–437.

Yick, K. Y., Torres, C. R., Peacock, T. & Stocker, R. 2009 Enhanced drag of a sphere settling in a stratified fluid at small Reynolds Number. *J. Fluid. Mech.* **632**, 49–68.